# LARGE DEFLECTION MODEL: IN-EXTENSIBLE CONDITION

4.1 Introduction

Under vibration conditions, a rotating system with hinge-roller support is subjected to deformation and it results in a movement of the roller support in an axial direction to fit the length of the shaft in the bending position. Thus, there is no straining of the shaft axis during the vibrations. This consideration of an inextensibility condition of the shaft axis introduces the nonlinear terms (i.e. Geometrical and Inertial nonlinear terms) in the equation of motion (Eqs.(4.9) -(4.10)).

Here, the investigation of bifurcations, stability and chaotic behavior of an elastically induced flexible rotating system has been studied which is subjected to an unbalance force due to an eccentricity and unbalance mass, as well as rub-impact phenomenon due to contact between the disk and casing. A non-dimensional equation of motion is formulated considering the inextensibility condition of the shaft axis. The free vibration analysis is also performed to analyze the effect of nonlinearities on the vibration characteristic of the rotating system.

4.2 Mathematical modeling (Phadatare et al., 2017)

A schematic diagram of a flexible shaft-disk system supported by hinge - roller guided support is shown in Fig.4.1. A cylindrical, uniform cross-sectional shaft having length L and diameter R_s rotates about the longitudinal axis at a speed Ω. The shaft holds a rigid disk along its span at various length L_d from the rear end of the shaft. The shaft is modeled by assuming the Euler-Bernoulli theorem and taking into account the effect of gravity, structural nonlinearity and inextensible condition while the shear deformation is considered to be neglected.
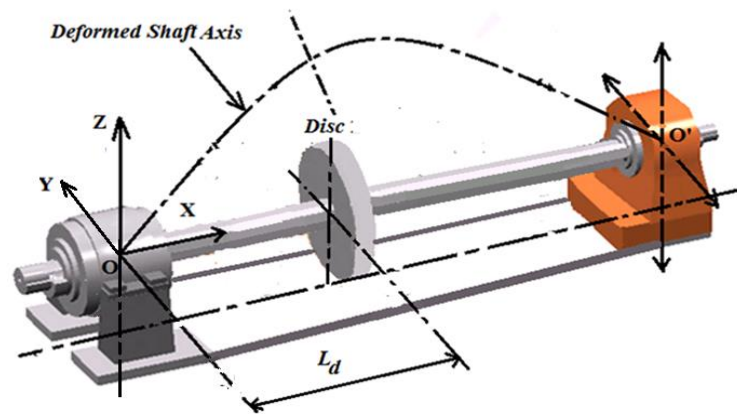
Fig.4.1: Graphical representation of flexible rotor-bearing consisting rotating shaft with rigid disk

The kinetic energy of the shaft and disk consist of two parts: translational and rotational energy.

a. *Kinetic energy of the shaft and disk*

The kinetic energy of the shaft can be expressed as

$$T_s = \frac{1}{2}\int_0^L \left(m(u_t^2 + v_t^2 + w_t^2) + I_1\omega_1^2 + I_2(\omega_2^2 + \omega_3^2) \right)dx. \tag{4.1}$$

$$T_d = \frac{1}{2}\int_0^L \left(M\{u_t^2 + v_t^2 + w_t^2\} + I_{1d}\omega_1^2 + I_{2d}\{\omega_2^2 + \omega_3^2\} \right)\delta(x - L_d)dx. \tag{4.2}$$

Here $I_1 = \int \rho(y^2 + z^2)dA$, $I_2 = \int \rho y^2 dA = \int \rho z^2 dA$. The subscripts x and t represents differentiation w.r.to x and t respectively, m and M are mass per unit length of the shaft and mass of disk respectively. I_1 and I_2 are the polar and diametrical mass moment of inertia of the shaft. Similarly, I_{1d} and I_{2d} represent the polar and diametrical moment of inertia of the disk. Displacements u, v and w respectively are along X, Y and Z coordinates system. Dirac delta function $\delta(x - L_d)$ has been used to represent the inertia effect of the rigid disk at a specific location, say L_d.
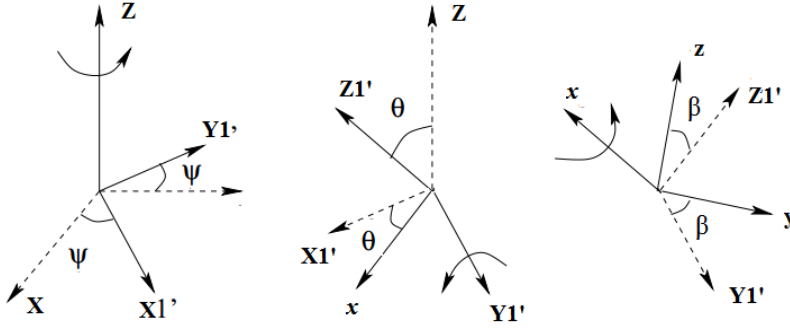

Fig.4.2: Euler angles rotation

The frame X–Y–Z is attached to the end of the shaft and considered as a global coordinate system. The frame x–y–z is a rotating frame, and the three successive Euler-angle rotations define its relationship with the global frame. Here, we considered rotation angles $\psi(x,t)$, $\theta(x,t)$ and $\beta(x,t)$, which are shown in Fig.4.2. The angle $\beta(x,t)$ is a total angle of rotations. It includes both torsional deformation $\phi(x,t)$ and shaft spinning angle Ωt.

Thus, ω can be expressed as following as similarly described in Section 3.2a

$$\omega = \omega_1 e_1 + \omega_2 e_2 + \omega_3 e_3. \tag{4.3}$$

Here, $\omega_1 = \beta_t - \psi_t \sin\theta$, $\omega_2 = \psi_t \sin\beta \cos\theta + \theta_t \cos\beta$, $\omega_3 = \psi_t \cos\beta \cos\theta - \theta_t \sin\beta$.

The effect of shear deformation is neglected, thus angles ψ and θ can be expressed in relation with the displacements as (Appendix A.1)

$$\psi = \frac{v_x}{\sqrt{(1+u_x)^2 + v_x^2}}, \quad \theta = \frac{-w_x}{\sqrt{(1+u_x)^2 + v_x^2 + w_x^2}}.$$

b. *Potential energy of the shaft*

The potential energy of the shaft can be expressed as (Nayfeh, 2008)

$$U_s = \int_0^L (A_{11}e\delta e + D_{11}\rho_1\delta\rho_1 + D_{22}\rho_2\delta\rho_2 + D_{22}\rho_3\delta\rho_3). \tag{4.4}$$

Here, A_{11} is axial rigidity; D_{11} and D_{22} are torsional and bending rigidity of the shaft. One of the ends of the shaft is roller-support so the end can be freely moved in the longitudinal direction. Thus, the inextensibility condition is considered here. The inextensibility condition considers zero strain (e) along the shaft length, and it can be expressed as (Nayfeh, 2008)

$$e = 0,$$
$$\because (1+u_x)^2 + v_x^2 + w_x^2 = 1. \tag{4.5}$$

Using the kinetic love analogy, the curvature ρ can be expressed as

$$\rho = \rho_1 e_1 + \rho_2 e_2 + \rho_3 e_3. \tag{4.6}$$

Here, $\rho_1 = \phi_x - \psi_x \sin\theta$, $\rho_2 = \psi_x \sin\phi\cos\theta + \theta_x \cos\phi$, $\rho_3 = \psi_x \cos\phi\cos\theta - \theta_x \sin\phi$.

c. Extended Hamiltonian principle

The total kinetic energy of the system can be $T = T_s + T_d$. Substituting Eqs.(4.3) and (4.6) into total kinetic energy of the system (T), and Eq.(4.5) into the strain energy (Eq. (4.4)) with some relevant relations as described in Appendix (A.1), Then applying the extended Hamiltonian principal $\{\int_{t_1}^{t_2}(\delta T - \delta U + \delta W_e)\,dt = 0\}$, to the total kinetic energy and the strain energy of shaft-disk elements, one may obtain the differential equation of motion of the rotating shaft-disk system

$$m(-v_{tt} - v_{xx}\int_L^x\int_0^x(v_{xt}^2 + v_{xtt}v_x + w_{xt}^2 + w_{xtt}w_x)dxdx - v_x\int_0^x(v_{xt}^2 + v_{xtt}v_x + w_{xt}^2 + w_{xtt}w_x)dx) - Mv_{tt}\mid_{x=L_d}$$

$$+M((-v_{xx}\int_L^x\int_0^x(v_{xt}^2 + v_{xtt}v_x + w_{xt}^2 + w_{xtt}w_x)dxdx - v_x\int_0^x(v_{xt}^2 + v_{xtt}v_x + w_{xt}^2 + w_{xtt}w_x)dx)\mid_{x=L_d}$$

$$+I_1\Omega(\frac{1}{2}w_x^2 w_{xxt} + w_x w_{xx}w_{xt} + w_{xxt} + v_x v_{xx}w_{xt} + \frac{1}{2}v_x^2\,w_{xxt}) + I_{1d}\Omega(\frac{1}{2}w_x^2 w_{xxt} + w_x w_{xx}w_{xt} + w_{xxt}$$

$$+v_x v_{xx}w_{xt} + \frac{1}{2}v_x^2 w_{xxt})\mid_{x=L_d} + I_1(\phi_t w_{xxt} + \phi_{tx}w_{xt} + w_x^2 v_{xxtt} + 2w_{xt}v_{xt}w_{xx} + \phi_{tt}w_{xx} + 2w_{xxt}v_{xxt}w_x$$

$$+2w_x v_{xtt}w_{xx} + \phi_{xxt}w_x + 2w_{xxt}v_{xt}w_x) + I_{1d}(\phi_t w_{xxt} + \phi_{tx}w_{xt} + w_x^2 v_{xxtt} + 2w_{xt}v_{xt}w_{xx} + \phi_{tt}w_{xx}$$

$$+2w_{xxt}v_{xxt}w_x + 2w_x v_{xtt}w_{xx} + \phi_{xxt}w_x + 2w_{xxt}v_{xt}w_x)\mid_{x=L_d} + I_2(v_{xxtt}v_x^2 + v_{xxtt} + v_x w_x w_{xxtt} + v_{xx}w_{xt}^2$$

$$+2v_{xtt}v_x v_{xx} + v_x w_{xx}w_{xtt} + 2v_{xt}v_x v_{xxt} + v_{xx}w_x w_{xtt} + v_{xt}^2 + 2v_x w_{xxt}w_{xt}) + I_{2d}(v_{xxtt}v_x^2 + v_{xxtt} + v_x w_x w_{xxtt}$$

$$+v_{xx}w_{xt}^2 + 2v_{xtt}v_x v_{xx} + v_x w_{xx}w_{xtt} + 2v_{xt}v_x v_{xxt} + v_{xx}w_x w_{xtt} + v_{xt}^2 + 2v_x w_{xxt}w_{xt})\mid_{x=L_d} - D_{11}(\phi_x w_x$$

$$+2\phi_{xx}w_{xx} + \phi_x w_{xxx} + 4w_x v_{xxx}w'' + w_x^2 v_{xxxx} + 2w_{xx}^2 v_{xx} + 2w_x v_{xx}w_{xxx}) - D_{22}(4v_x v_{xx}v_{xxx} + w_x v_x w_{xxx}$$

$$+w_x v_{xx}w_{xxx} + 3v_x w_{xx}w_{xxx} + v_{xx}w_{xx}^2 + v_{xx}^3 + v_x^3 v_{xxxx} + v_{xxxx}) = 0, \tag{4.7}$$

$$m\left(-w_{tt} - w_{xx}\int_L^x\int_0^x(v_{xt}^2 + v_{xtt}v_x + w_{xt}^2 + w_{xtt}w_x)dxdx - w_x\int_0^x(v_{xt}^2 + v_{xtt}v_x + w_{xt}^2 + w_{xtt}w_x)dx\right) -$$

$$Mw_{tt}\mid_{x=L_d} + M\left(-w_{xx}\int_L^x\int_0^x(v_{xt}^2 + v_{xtt}v_x + w_{xt}^2 + w_{xtt}w_x)dxdx - w_x\int_0^x(v_{xt}^2 + v_{xtt}v_x + w_{xt}^2 + w_{xtt}w_x)dx\right)\mid_{x=L_d}$$

$$-I_1\Omega(\frac{1}{2}v_x^2 v_{xxt} + v_x v_{xx}v_{xt} + v_{xxt} + w_x w_{xx}v_{xt} + \frac{1}{2}w_x^2 v_{xxt}) - I_{1d}\Omega(\frac{1}{2}v_x^2 v_{xxt} + v_x v_{xx}v_{xt} + v_{xxt} + w_x w_{xx}v_{xt}$$

$$+\frac{1}{2}w_x^2 v_{xxt})\mid_{x=L_d} - I_1\left(\phi_t v_{xxt} + \phi_{xt}v_{xt} + v_x^2 w_{xxtt} + 2v_{xt}w_{xt}v_{xx} + \ddot{\phi}_{tt}v_{xx} + 2v_{xt}w_{xxt}v_x + 2v_x w_{xtt}v_{xx} + \phi_{xxt}v_x$$

$$+2v_{xxt}w_{xt}v_x\right) - I_{1d}\left(\phi_t v_{xxt} + \phi_{xt}v_{xt} + v_x^2 w_{xxtt} + 2v_{xt}w_{xt}v_{xx} + \ddot{\phi}_{tt}v_{xx} + 2v_{xt}w_{xxt}v_x + 2v_x w_{xtt}v_{xx} + \phi_{xxt}v_x$$

$$+2v_{xxt}w_{xt}v_x\right)\mid_{x=L_d} + I_2\left(w_{xxtt}w_x^2 + w_{xxtt} + w_x v_x v_{xxtt} + w_{xx}\dot{v}_{xt}^2 + 2w_{xtt}w_x w_{xx} + w_x v_{xx}v_{xtt} + 2w_{xt}w_x w_{xxt}$$

$$+w_{xx}v_x v_{xtt} + w_{xt}^2 + 2w_x v_{xxt}v_{xt}\right) + I_{2d}\left(w_{xxtt}w_x^2 + w_{xxtt} + w_x v_x v_{xxtt} + w_{xx}\dot{v}_{xt}^2 + 2w_{xtt}w_x w_{xx} + w_x v_{xx}v_{xtt}$$

$$+2w_{xt}w_x w_{xxt} + w_{xx}v_x v_{xtt} + w_{xt}^2 + 2w_x v_{xxt}v_{xt}\right)\mid_{x=L_d} - D_{11}(\phi_{xxx}v_x + 2\phi_{xx}v_{xx} + \phi_x v_{xxx} + 4v_x w_{xxx}v_{xx}$$

$$+v_x^2 w_{xxxx} + 2v_{xx}^2 w_{xx} + 2v_x w_{xx}v_{xxx}) - D_{22}(4w_x w_{xx}w_{xxx} + v_x w_x v_{xxxx} + v_x w_{xx}v_{xxx} + 3w_x v_{xx}v_{xxx}$$

$$+w_{xx}v_{xx}^2 + w_{xx}^3 + w_x^2 w_{xxxx} + w_{xxxx}) = 0. \tag{4.8}$$

$$(\phi_{tt} - v_{xtt}w_x - w_{xt}v_{xt}) + D_{11}(w_x v_{xxx} + v_{xx}w_{xx} + \phi_{xx})(I_1 + I_{1d}\delta(x-L_d)) = 0.$$

Boundary conditions at $x = 0$ and $x = L$ are
$$v = 0, \quad D_{11}(\phi_x w_x + w_x^2 v_{xx}) + D_{22}v_{xx} = 0,$$
$$w = 0, \quad D_{22}w_{xx} = 0,$$
$$\phi = 0.$$

In comparison to the flexural inertia and stiffness terms, one may neglect the torsional inertia terms (ϕ) which is expressed as $\phi = -\int_0^x w_x v_{xx}dx + \ldots$. The effect of nonlinear terms due to the rotary inertia can also be neglected as the shaft element is considered to be slender. Following non-dimensional quantities are used for further analysis.

$$x^* = \frac{x}{L}, \quad v^* = \frac{v}{L}, \quad w^* = \frac{w}{L}, \quad \Omega^* = \sqrt{\frac{mL^4}{D_{22}}}\Omega, \quad t^* = \sqrt{\frac{D_{22}}{mL^4}}t, \quad M = \frac{M_d}{mL}, I_2^* = \frac{I_2}{mL^2},$$

$$I_{2d}^* = \frac{I_{2d}}{mL^3}, \quad c^* = \frac{cL^2}{\sqrt{mD_{22}}}.$$

Substituting expressions of ϕ and non-dimensional quantities into the dimensional Eqs.(4.7) and (4.8) and considering $I_1 = 2I_2$, one may obtain the nonlinear non-dimensional equations by dropping the asterisk from the non-dimensional terms and neglecting the effect of torsional inertia.

$$v_{tt} + v_{xx}\int_1^x\int_0^x(v_{xt}^2 + v_{xtt}v_x + w_{xt}^2 + w_{xtt}w_x)dxdx + v_x\int_0^x(v_{xt}^2 + v_{xtt}v_x + w_{xt}^2 + w_{xtt}w_x)dx) -$$

$$I_2(2\Omega w_{xxt} + v_{xxtt}) + M\left(v_{tt} + v_{xx}\int_1^x\int_0^x(v_{xt}^2 + v_{xtt}v_x + w_{xt}^2 + w_{xtt}w_x)dxdx\right)\delta(x - L_d) +$$

$$M\left(v_x\int_0^x(v_{xt}^2 + v_{xtt}v_x + w_{xt}^2 + w_{xtt}w_x)dx\right)\delta(x - L_d) - I_{2d}(2\Omega w_{xxt} + v_{xxtt})\delta(x - L_d) + cv_t +$$

$$v_x^2 v_{xxxx} + v_x w_x w_{xxxx} + 3v_x w_{xx}w_{xxx} + v_{xx}w_{xx}^2 + v_x^3 + v_{xxxx} + w_x v_{xx}w_{xxx} + 4v_x v_{xx}v_{xxx} = 0.$$

(4.9)

$$w_{tt} + w_{xx}\int_1^x\int_0^x(v_{xt}^2 + v_{xtt}v_x + w_{xt}^2 + w_{xtt}w_x)dxdx + w_x\int_0^x(v_{xt}^2 + v_{xtt}v_x + w_{xt}^2 + w_{xtt}w_x)dx +$$

$$I_2(2\Omega v_{xxt} - w_{xxtt}) + M\left(w_{tt} + w_{xx}\int_1^x\int_0^x(v_{xt}^2 + v_{xtt}v_x + w_{xt}^2 + w_{xtt}w_x)dxdx\right)\delta(x - L_d) +$$

$$M\left(w_x\int_0^x(v_{xt}^2 + v_{xtt}v_x + w_{xt}^2 + w_{xtt}w_x)dx\right)\delta(x - L_d) + I_{2d}(2\Omega v_{xxt} - \ddot{w}_{xxtt})\delta(x - L_d) + cw_t +$$

$$w_x^2 w_{xxxx} + w_x v_x v_{xxxx} + 3w_x v_{xx}v_{xxx} + w_{xx}v_{xx}^2 + w_x^3 + w_{xxxx} + v_x w_{xx}v_{xxx} + 4w_x w_{xx}w_{xxx} = 0.$$

(4.10)

The boundary conditions are rewritten as below

$$v = 0, \quad v_{xx} = 0, \quad w = 0, \quad w_{xx} = 0 \quad \text{at} \quad x = 0 \quad \text{and} \quad x = 1.$$

4.3 Free vibration analysis of the nonlinear shaft disk system

4.3.1 Analysis

Considering the single mode the Galerkin's approach, the partial differential equations of motion is discretized into temporal equations of motion by using following eigen functions.

$$v(x,t) = \varphi(x)V(t), \qquad w(x,t) = \varphi(x)W(t). \tag{4.11}$$

Here, $\varphi(x) = \sqrt{2}\sin(\pi x)$, is the admissible function obtained by satisfying the boundary conditions stated earlier, whereas V and W are time modulations representing the approximate solution of nonlinear oscillations. Substituting Eq. (4.11) into Eqs. (4.9) and (4.10), and then using the orthogonal properties of the mode shape, the discretized equations of motion become:

$$(A_1 + A_{1d})V_{tt} + cA_2V_t + A_3V + A_5(V^3 + VW^2) + (A_6 + A_{6d})(VV_t^2 + VW_t^2 + V^2V_{tt} + VWW_{tt})$$
$$-2\Omega(A_4 + A_{4d})W_t = 0. \tag{4.12}$$

$$(A_1 + A_{1d})W_{tt} + cA_2W_t + A_3W + A_5(W^3 + V^2W) + (A_6 + A_{6d})(WV_t^2 + WW_t^2 + VWV_{tt}$$
$$+ W^2W_{tt}) + 2\Omega(A_4 + A_{4d})V_t = 0 \tag{4.13}$$

Here,

$$A_1 = 1 + \pi^2 I_2; \quad A_{1d} = 2M\sin^2(\pi L_d) + 2I_{2d}\pi^2\sin^2(\pi L_d); \quad A_2 = 1; A_3 = \pi^6; \quad A_4 = \pi^2 I_2;$$

$$A_{4d} = 2\pi^2 I_{2d}\sin^2(\pi L_d); \quad A_5 = \pi^6; A_6 = -\left(\frac{3\pi^2}{8} - \frac{\pi^4}{3}\right);$$

$$A_{6d} = -[2M\pi^2\sin^2(\pi L_d)\left(\frac{\pi^2 L_d^2}{2} + \frac{\sin^2(\pi L_d)}{2} - \frac{\pi^2}{2}\right) - M\pi^2\cos(\pi L_d)\sin(\pi L_d)\sin 2(\pi L_d) + 2(\pi L_d)].$$

A similar method of the multiple scales as described in the Chapter 3 is applied here and it results in following equations for order ε^1

$O(\varepsilon^1)$

$$(A_1 + A_{1d})D_0^2 V_3 + A_3 V_3 - 2\Omega(A_4 + A_{4d})D_0 W_3 = -2(A_1 + A_{1d})D_0 D_2 V_1 - A_2 c D_0 V_1$$
$$+2(A_4 + A_{4d})\Omega D_2 W_1 - A_5 V_1^3 - A_5 V_1 W_1^2 - 2(A_6 + A_{6d})(D_0^2 V_1^3 + D_0^2 V_1 W_1^2). \tag{4.14}$$

$$(A_1 + A_{1d})D_0^2 W_3 + A_3 W_3 + 2\Omega(A_4 + A_{4d})D_0 V_3 = -2(A_1 + A_{1d})D_0 D_2 W_1 - A_2 c D_0 W_1$$
$$-2(A_4 + A_{4d})\Omega D_2 V_1 - A_5 W_1^3 - A_5 W_1 V_1^2 - 2(A_6 + A_{6d})(D_0^2 W_1^3 + D_0^2 W_1 V_1^2). \tag{4.15}$$

Here, the forward/backward natural frequency can be expressed as

$$N_{f,b} = \frac{\Omega(A_4 + A_{4d}) \pm \sqrt{\Omega^2(A_4 + A_{4d})^2 + A_3(A_1 + A_{1d})}}{A_1 + A_{1d}}. \tag{4.16}$$

After some manipulation, one may receive the following expressions as a solvability condition,

$$\begin{bmatrix} A_3 - (A_1 + A_{1d})N_f^2 & R_1(T_2) \\ -2i\Omega(A_4 + A_{4d})N_f & R_2(T_2) \end{bmatrix} = 0 \quad , \qquad \begin{bmatrix} A_3 - (A_1 + A_{1d})N_b^2 & S_1(T_2) \\ -2i\Omega(A_4 + A_{4d})N_b & S_2(T_2) \end{bmatrix} = 0 \quad . \tag{4.17}$$

Using the solvability condition, one may get a set of equations as

$$i\Gamma_1 D_2 F_1(T_2) - 2iA_2 c N_f F_1(T_2) - 8A_5 F_1(T_2)^2 \bar{F}_1(T_2) + \zeta F_1(T_2) F_2(T_2) \bar{F}_2(T_2) = 0 \quad . \tag{4.18}$$

$$i\Gamma_2 D_2 F_2(T_2) - 2iA_2 c N_b F_2(T_2) - 8A_5 F_2(T_2)^2 \bar{F}_2(T_2) + \zeta F_1(T_2) F_2(T_2) \bar{F}_1(T_2) = 0 \quad . \tag{4.19}$$

Here,

$$\Gamma_1 = 4\big((A_4 + A_{4d})\Omega - (A_1 + A_{1d})N_f\big), \quad \Gamma_2 = 4\big((A_4 + A_{4d})\Omega + (A_1 + A_{1d})N_b\big) \quad .$$

$$\zeta = 4(A_6 + A_{6d})(N_f + N_b)^2 - 16A_5 \quad .$$

Substituting the solutions of F_1 and F_2 in the polar form i.e., $F_n = (1/2)a_n \exp(i\Phi_n)$ where $n = 1, 2$ in the above equations and then solving resultant equations (by separating real and imaginary parts). After this manipulation, we can obtain the values for a_n and Φ_n. Back substituting theses values (i.e. a_n and Φ_n) in the solutions of ε^0 order equations, one may obtain the following expressions for the displacements v and w in Y and Z directions, respectively for the rotor-bearing system.

$$v = \phi(x)[A_f \cos(Q_{11}A_b^2 + Q_{22}A_f^2 + C_3 + N_f T_0) + A_b \cos(Q_{33}A_f^2 + Q_{44}A_b^2 + C_4 + N_b T_0)]. \tag{4.20}$$

$$w = \phi(x)[A_f \sin(Q_{11}A_b^2 + Q_{22}A_f^2 + C_3 + N_f T_0) + A_b \sin(Q_{33}A_f^2 + Q_{44}A_b^2 + C_4 + N_b T_0)] \quad . \tag{4.21}$$

Where

$$A_f = C_1 e^{P_1 T_0}; \qquad A_b = C_2 e^{P_2 T_0}; \qquad P_1 = \frac{A_2 c N_f}{\Gamma_1}; \quad P_2 = \frac{A_2 c N_b}{\Gamma_2}; \quad Q_{11} = \frac{\zeta \Gamma_2}{2\Gamma_1 c N_b}; \quad Q_{22} = -\frac{2A_5}{A_2 c N_f};$$

$$Q_{33} = \frac{\zeta \Gamma_1}{2\Gamma_2 c N_f}; \quad Q_{44} = -\frac{2A_5}{A_2 c N_b}.$$

Here, C_1, C_2, C_3, and C_4 are integration constants determined by the initial conditions for the free vibration analysis. Newton-Rapson scheme has been adopted here. Both the forward and backward frequencies are excited, and the above equations depict the free vibration of the system with geometrical and inertial nonlinearities. A distinct and different closed form solution are obtained for finding the backward and forward natural frequencies for the rotor-bearing system which are not earlier explored with reference to the solutions obtained for the system with a shaft element only. The Fourier spectrum and Poincare section have been illustrated to deepen the behavioral pattern of dynamic responses.

4.3.2 Results and Discussions

Here, the parameters of the rotating system are taken as : Shaft length ($L = 1$), Disk mass ($M=1.5$), Disk position ($L_d=L/3$), Damping ($c= 0.05$) Moment of inertia ($I_2 =0.000625$). Initially, the time history has been portrayed in order to rectify the correctness of the fundamental concept of kinematics in deriving the mathematical model and computational procedures adopted in this

present work. The exact solution has been obtained by numerically integrating the governing equations of motion (Eqs. (4.7)-(4.8))).
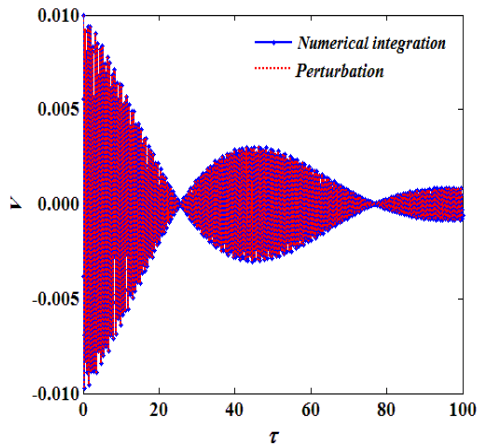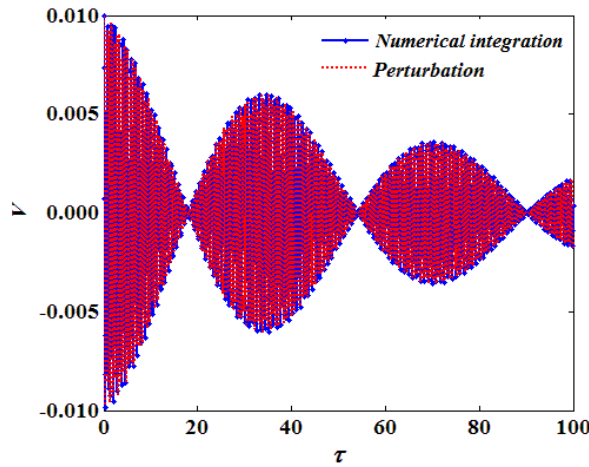

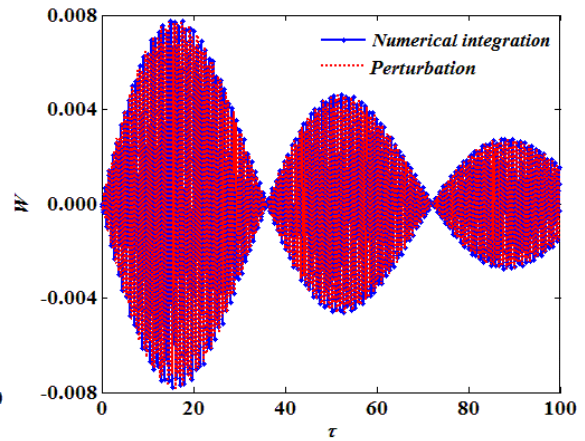**Fig.4.3:** Time history for rotating shaft without disk effect in Y direction (v) for Ω = 10 Hz.
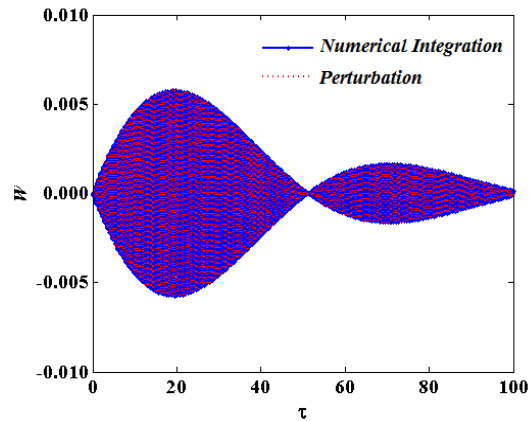
Fig.4.4: Time history for rotating shaft without disk effect in Z direction (w) for Ω = 10 Hz,

Figures 4.3 and 4.4 depict the numerical integration and perturbation time history for the shaft element at the mid-point displacements for V and W, and it has been found that the obtained results are in a very good agreement. The initial conditions are considered here as $V(0) = 0.01$. It has been observed that though, the input excitation has been given only in one plane i.e., X – Y plane, an effect of the excitation has also been observed in x - z plane as well due to the strong gyroscopic effect and the geometrical coupling in both the shaft and disk elements. The period of beating i.e., time taken between the points of maximum amplitude is unlike for two different vibration responses of V and W while the beating period for the vibration in W is observed to be less than the period of V as the frequency of shaft speed is closer to the forward natural frequency as N_f - Ω = 2. The reduction rate of the vibration amplitude is higher for the responses of w than the counter-part V as the excitation occurs in X-Y plane.

The time histories for the rotor-bearing system are illustrated in Fig.4.5 and Fig.4.6, considering the same initial conditions as that of obtained for $M = 1.5$ and $I_2 = 0.00625$. The perturbation result obtained from Eqs.(4.20)-(4.21) are verified with the exact solution for the system and it is found that the perturbation solution agrees well with the numerical integration solutions. A comparison between the amplitudes of V and W for the system with and without the disk is shown in Fig.4.7 and Fig.4.8. It can be noted that due to the additional inertia effect of the disk, the settling time is observed to be higher for the system without the disk and time taken by the system to damp out increases. Furthermore, the beating period is noted to be higher for the vibration of V i.e., the response in Y direction than the vibration of W i.e., the response in Z direction. The amplitude of vibration reduction is observed to be higher for the response of W as the response of W is out-of-plane vibration in nature.
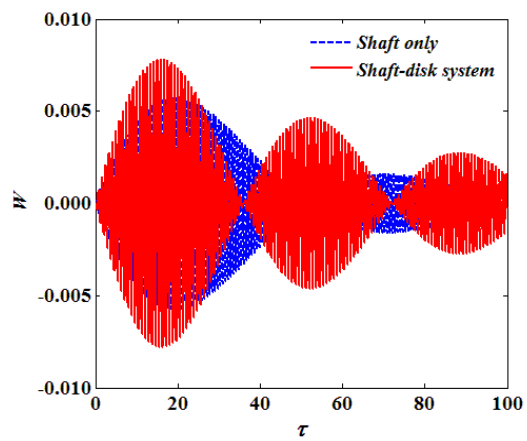
Fig.4.5: Time history for rotating shaft without disk effect in *Y* direction (*v*) for Ω = 10 *Hz*

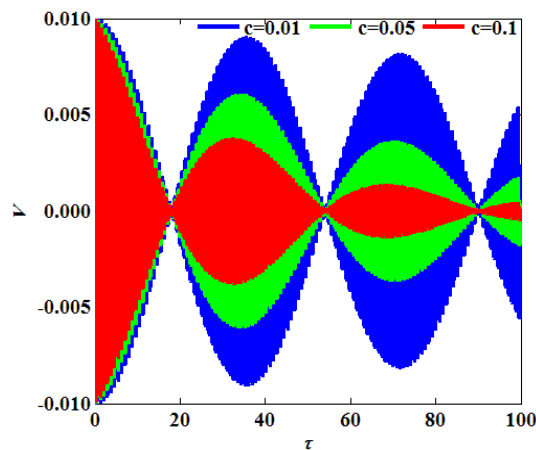**Fig.4.6:** Time history for rotating shaft without disk effect in *Z* direction (*w*) for Ω = 10 *Hz*

.
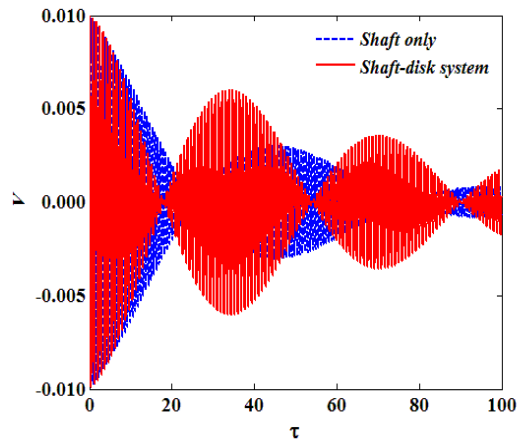
Fig.4.7: Time history for rotating shaft with and without disk system in *Y* direction (*v*) for Ω = 10 *Hz*, and *M* =1.5.

Fig.4.8: Time history for rotating shaft with and without disk system in *Z* direction (*w*) for Ω = 10 *Hz*, and *M* =1.5.

Fig.4.9: Time history for rotor-bearing system in *Y* direction for Ω= 10 *Hz*, *M* = 1.5 and I_2 =0.00625
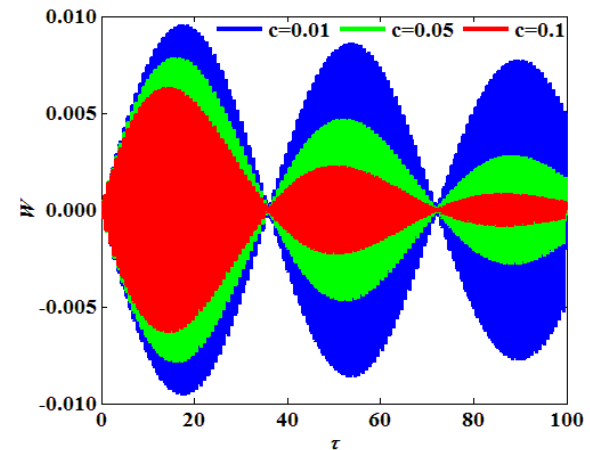
Fig.4.10: Time history for rotor-bearing system in *Z* direction for Ω = 10 *Hz*, *M* = 1.5 and I_2 =0.00625

The effect of damping on the dynamic behaviors has been portrayed in Fig.4.9 and Fig.4.10 and clear evidence has been noticed that a reduction in the vibration amplitude has been observed as

expected in both responses of *V* and *W* with an increase in the damping. Hence, the system becomes stable or the vibration can be restricted under a moderately high value of the damping constant. It is interesting to note that the beating period does not influenced by increasing the damping constant of the system as the damped natural frequencies remain almost unchanged. The Campbell diagram (Fig.4.11) used to display the forward N_f and backward N_b natural frequencies with respect to rotational speed (Ω) for different values of I_2 in the absence of the disk which is in accordance with the outcomes represented in [Hosseini et al 2009]. The variation of N_f and N_b of the shaft-disk system with Ω is also depicted in Fig.4.12. With increase in rotational speed (Ω), both N_f and N_b increase while with decrease in I_2, both N_f and N_b are decreased to a lower value with Ω.
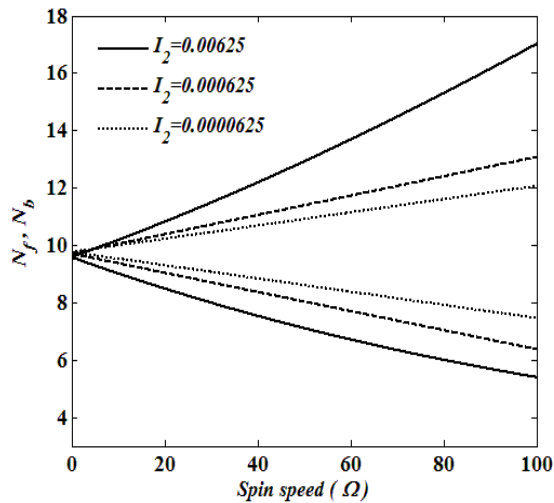
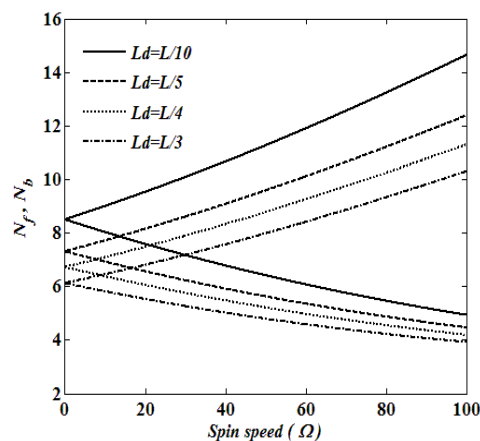Fig.4.11: Forward and backward natural frequencies of shaft element only.
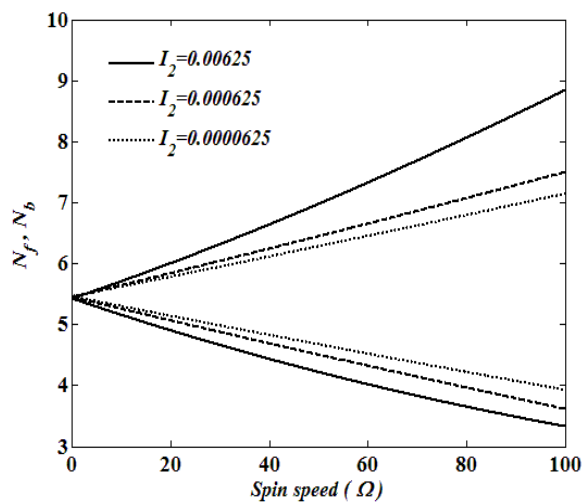
Fig.4.12: Forward and backward natural frequencies of shaft with disk element for M = 1.5 and L_d = L/3

In Fig.4.13, N_f and N_b for the rotor-bearing are plotted for different values of the mass ratio *M*. It is observed from the figure that the rate of increasing N_f and N_b decreases with increase in mass of the disk and hence, the unstable frequency of the system decreases with increase in *M*.
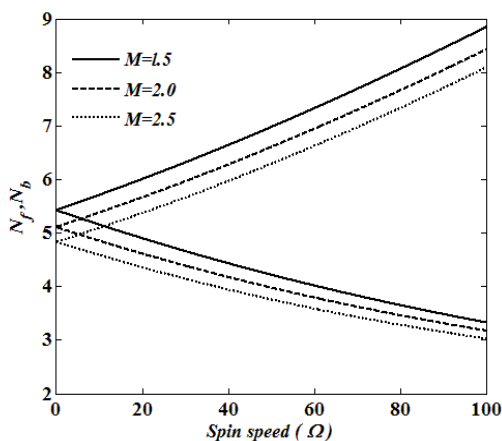
Fig.4.13: Effect of mass ratio (*M*) on forward and backward natural frequencies of shaft with disk system for I_2 =0.00625
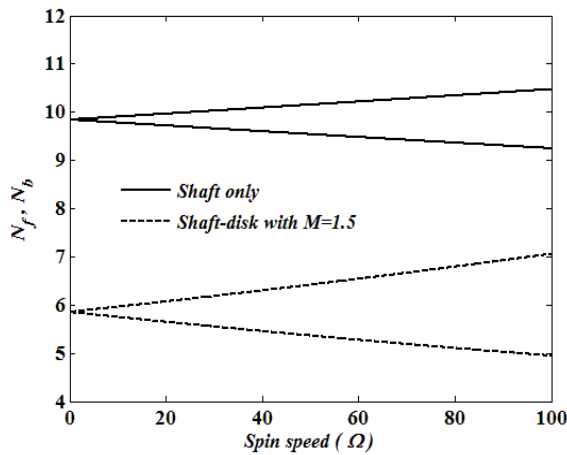
Fig.4.14: Effect of disk location L_d on forward and backward natural frequencies of shaft with disk system for *M* = 1.5 and I_2 =0.00625

With an increase in the mass ratio *M*, the critical speed starts at a lower value and the slope i.e, rate $dN/d\varphi$ of the diagram has a slight change. Hence, it has been observed that rate of changing the forward ($dN_f/d\varphi$) and the backward ($dN_b/d\varphi$) natural frequencies is quite similar but in reverse directions. Furthermore, differences of the forward and backward natural frequencies

with a mean speed are almost same in a magnitude. From Fig.4.14, it can be observed that the forward and backward linear natural frequencies rely not only upon mass moment of inertia (I_2), rotational speed (Ω), mass ratio (M) of the disk and the shaft, but also upon the position of the disk (L_d) along the shaft length. An influence of the disk location along the shaft is illustrated in Fig.4.14 and it is noted that the slope ($dN_f/d\varphi$) gets higher as compared to the slope ($dN_b/d\varphi$). It is observed that the rate of change of the frequency increases as the disk is moved away from the mid-point of the shaft. The maximum natural frequency has been ascertained at a condition when the location of the disk is closer to either of the bearing ends. This configuration may reduce the rotor-bearing system to the shaft system and the values of the fundamental natural frequencies are similar to that of the values for the shaft element alone as the effective mass of the system remains almost the same.
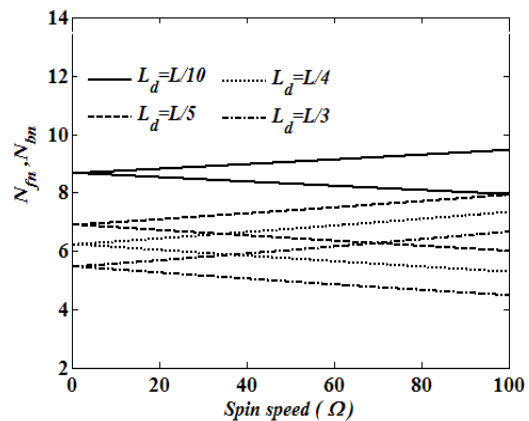

Fig.4.15: Forward and backward natural frequencies of shaft with and without disk I_2 = 0.000625.
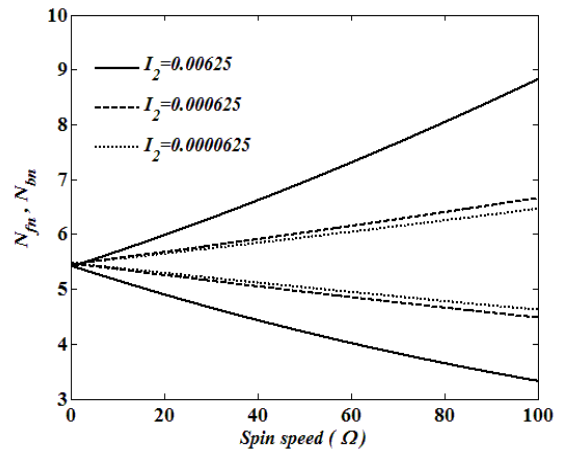
Fig.4.16: Influence of mass of moment of inertia (I_2) on nonlinear forward and backward natural frequencies of rotor-bearing system M= 1.5.
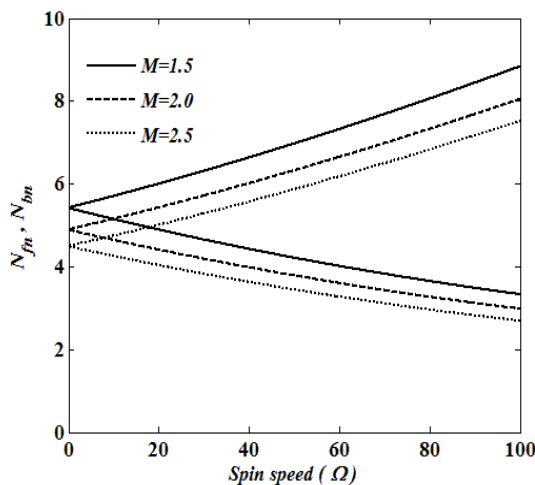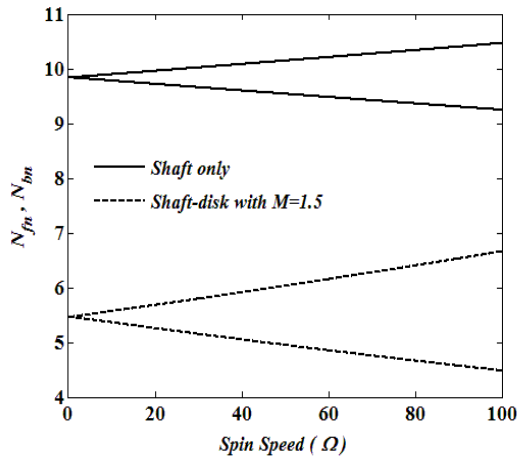

Fig.4.17: Influence of mass ratio (M) on nonlinear forward and backward natural frequencies of rotor-bearing system for I_2 = 0.00625 and L_d =L/3


Fig.4.18: Effect of disk location (L_d) on nonlinear forward and backward natural frequencies of shaft with disk system; M= 1.5 and I_2 = 0.000625

Figures 4.16–4.18 show the first mode of vibration representing N_{fn} and N_{bn} with Ω for the parameters I_2, M and L_d, respectively. Due to the gyroscopic effect, the change of N_{fn} and N_{bn} is significant at a higher value of I_2. Unlike the linear part, the length between N_{fn} and N_{bn} is more

prominent and large for a variation of the diametrical mass moment of inertia. The rotor-bearing system experiences lower nonlinear natural frequencies when the mass ratio gets increased as the inertia of the disk increases with an effect of the high rotational displacement. The effect of varying the disk location leads to a significant effort of finding the nonlinear frequencies in a response to the linear frequencies. It is true that there is an effect of the nonlinearity for calculating the natural frequencies at a location of the disk near to the mid-point of the shaft due to large geometric deflection of the flexible shaft. Figure 4.19 compares N_{fn} and N_{bn} for the rotating shaft with and without the disk. It is identified that the rate of $dN_{fn}/d\varphi$ and $dN_{bn}/d\varphi$ is more for the combined system than that of the shaft alone. Finally, it is observed that the natural frequency for the combined system is always less than for the shaft alone.
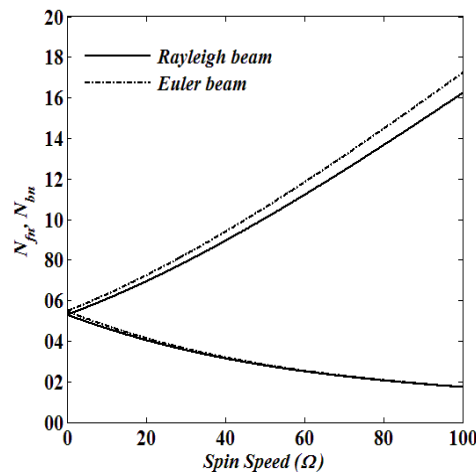

Fig.4.19: Nonlinear forward and backward natural frequencies for the system with and without disk for $I_2 = 0.000625$ and $L_d = L/3$.
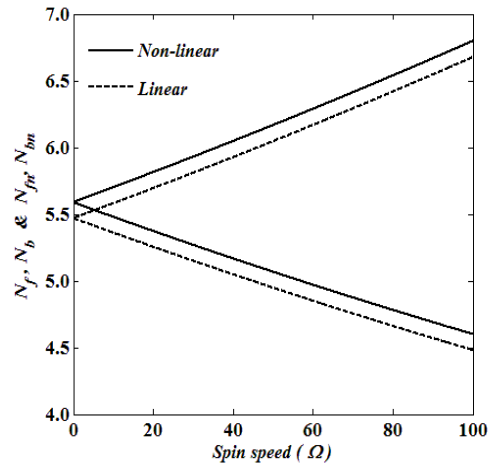
Fig.4.20: Frequency diagram to indicate the differences between linear and nonlinear forward and backward natural frequencies for $M= 1.5$, $I_2 = 0.000625$ and $L_d = L/3$
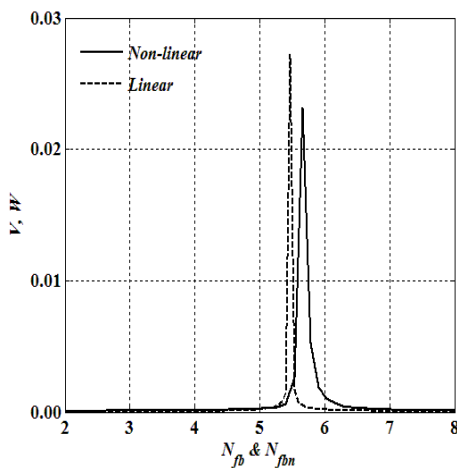
Fig.4.21: Fourier spectrum at a spin speed ($\Omega = 0$) for $M= 1.5$, $I_2 = 0.000625$ and $L_d = L/3$

Fig. 4.22: Influence of rotary inertia on nonlinear forward and backward natural frequencies of rotor-bearing system for $I_2 = 0.0225$ and $L_d = L/3$.

Figures 4.20-4.21 show the effect on the natural frequency of the system due to consideration of the nonlinear terms causing phenomena like the hardening effect. It is clearly observed from Figs.4.20 and 4.21 that the geometric nonlinearity gives rise to distinct and separate values of the natural frequencies as compared to the linear case. In addition, it is worthy to note that the whirling speeds show an error of 5-8% for the linear systems. Hence, for the high speed

applications, an accurate understanding of the natural frequencies is highly significant else the system may undergo catastrophic failure under a slight variation of the rotational frequency.

Figure 4.22 shows the influence of the rotary inertia effect on the nonlinear natural frequencies of the rotor system for I_2 = 0.0225. Here, it has been found that the inclusion of the rotary inertia term imparts a significant effect on the natural frequencies of the system such as softening effect. As well as the slope of nonlinear forward natural frequencies (N_{fn}) with respect to the spins speed (Ω) is comparatively less for the Rayleigh's beam model as compared to that of the Euler's beam model. This softening effect increases with the spin speed (Ω) for the nonlinear forward natural frequencies (N_{fn}) but not for the nonlinear backward natural frequencies (N_{bn}). The error between the results of these two beam models lies in 4–6% range.
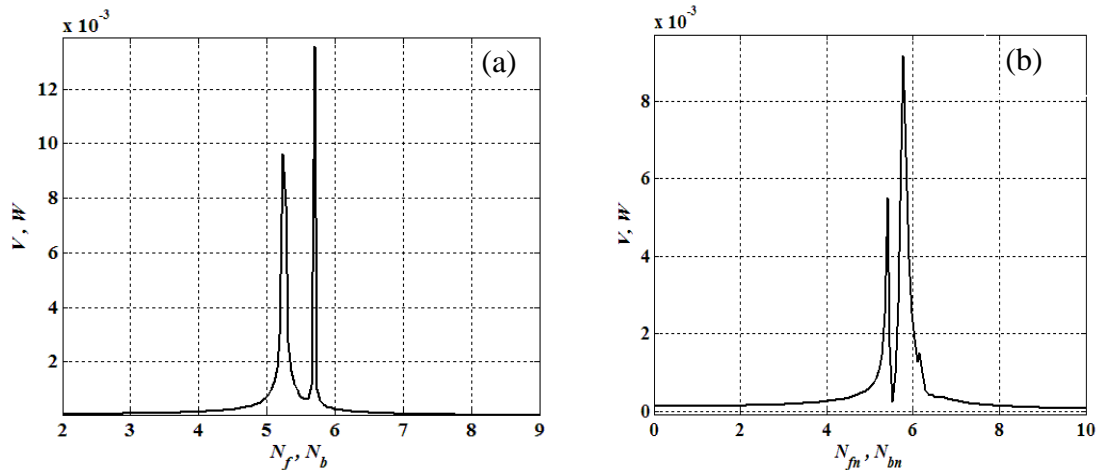

Fig.4.23: Fourier spectrum at a spin speed Ω = 20 *rad/s* (a) Linear case (b) Nonlinear case

Hence, the theoretical rotor model with the rotary inertia (Rayleigh's beam model) can be useful in a rotor systems for a large diametrical inertia and conversely, the theoretical rotor model without the rotary inertia (Euler's beam model) is sufficient for rotor models with smaller diametrical inertia to analyze the natural frequency of the rotating systems for a specific rotational speed (Ω) and found to be in a good agreement with the finding through the Campbell diagrams. This hardening effect i.e., an increase in the natural frequencies is also shown in Figs.4.23 - 4.25.
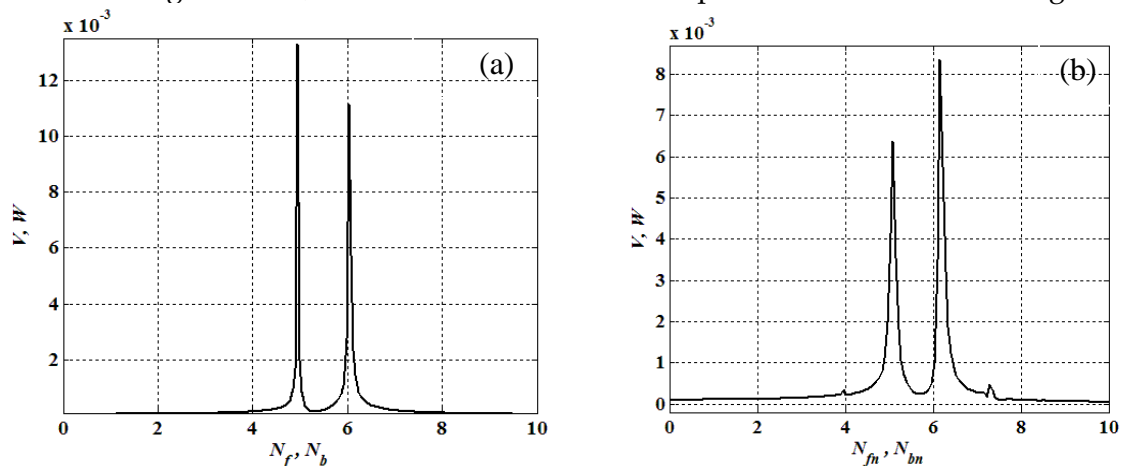

Fig.4.24: Fourier spectrum at a spin speed Ω = 50 *rad/s* (a) Linear case (b) Nonlinear case.

It has been observed that for a lower value of the rotational speed, the forward natural frequency gets dominated for the both cases as the maximum amplitude of vibration is observed for the condition where the rotational speed matches with the forward natural frequency. However, for a higher value of the spin speed, while the backward natural frequency gets dominated for the linear analysis, and the forward natural frequency is seen to be dominated in the nonlinear condition. In addition, the maximum amplitude of vibration is always observed to be higher for the linear case as compared to the nonlinear analysis. The equations expressed as $N_{fn} = Q_{11}A_b^2 + Q_{22}A_f^2 - N_f$ and $N_{bn} = Q_{33}A_f^2 + Q_{44}A_b^2 - N_b$ are used to obtain the nonlinear natural frequencies. Since A_b^2 and A_f^2 are dependent on initial conditions, the values of nonlinear natural frequencies are being evolved under changing of the initial conditions clearly shown in 4.26. Figure 4.26 illustrates the effect of initial conditions to determine the natural frequencies. Here initial conditions as $a) v = 0.001; v_t = 0; w = 0;$ and $w_t = 0, b) v = 0.01; v_t = 0.01; w = 0;$ and $w_t = 0$ have been used for demonstrating its effect.

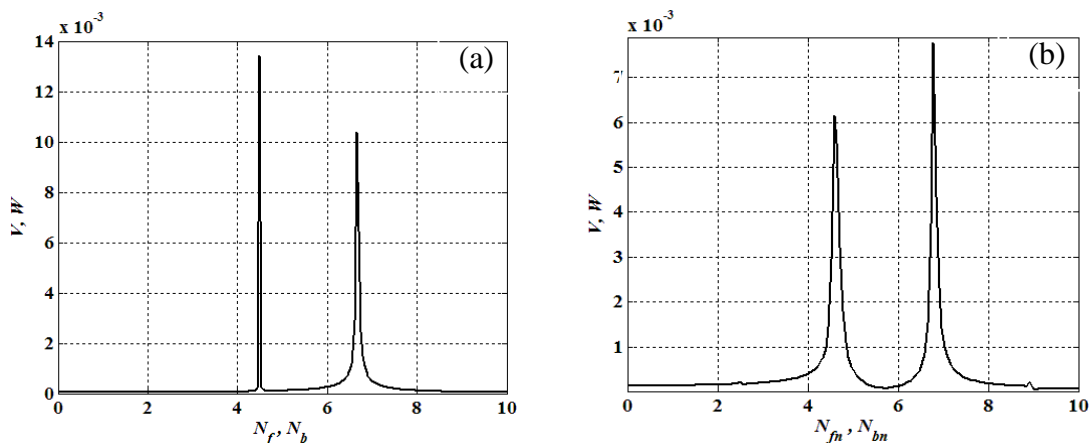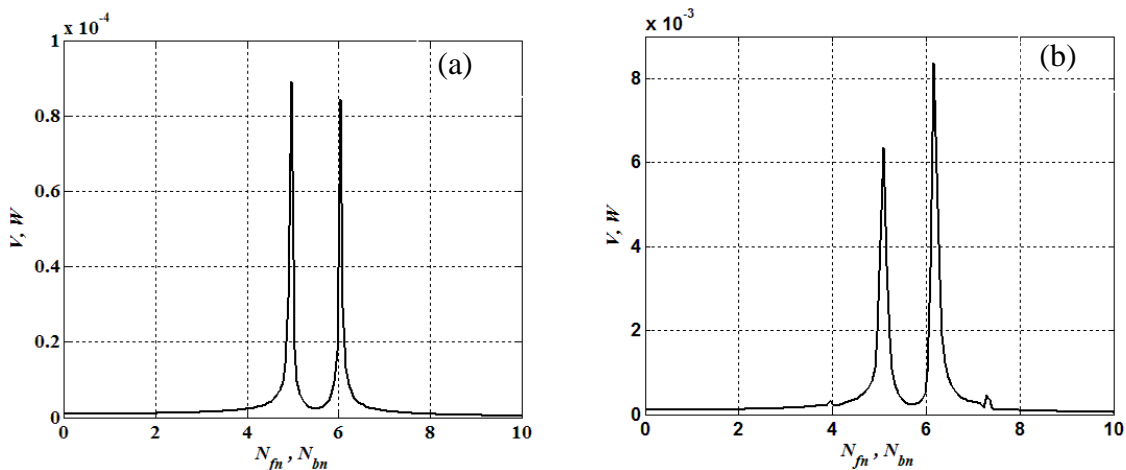**Fig.4.25:** Fourier spectrum at a spin speed Ω = 100 *rad/s* (a) Linear case (b) Nonlinear case.

Fig.4.26: Influences of initial conditions on the nonlinear Natural frequencies at a spin speedΩ = 50 *rad/s*

The nonlinear transient behavior of the rotor-bearing system with and without damping is being illustrated in Figs. 4.27 - 4.30. A periodic response has been observed for the system with the spin speed equal to zero, while the effect of gyroscopic becomes significant for every non-zero shaft speed. A single point on the Poincare section of Fig. 4.27 depicts a periodic motion of the system.

However, Fig.4.28 shows a gradual decrease in the amplitude of oscillations, which indicates a loss of the energy during the oscillatory motion so the system is reached eventually to a rest position. Hence the origin is called a stable node; the motion is simply stable and not asymptotically stable. Figures 4.29 and 4.30 show the presence two frequencies with an evidence

of beat phenomenon in the time series plot. The Poincare's map shows the presence of a quasi-periodic motion of the present system at certain spinning speed.
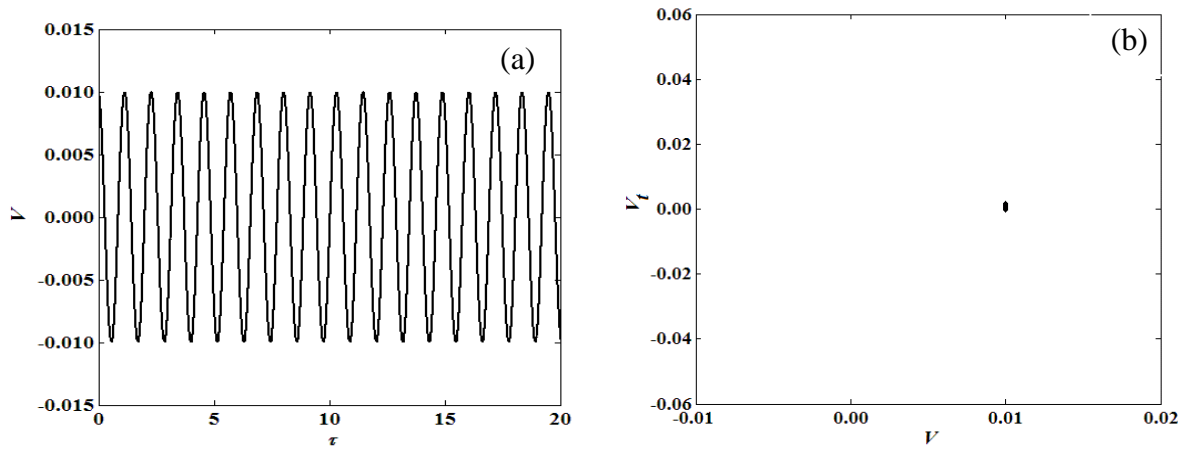

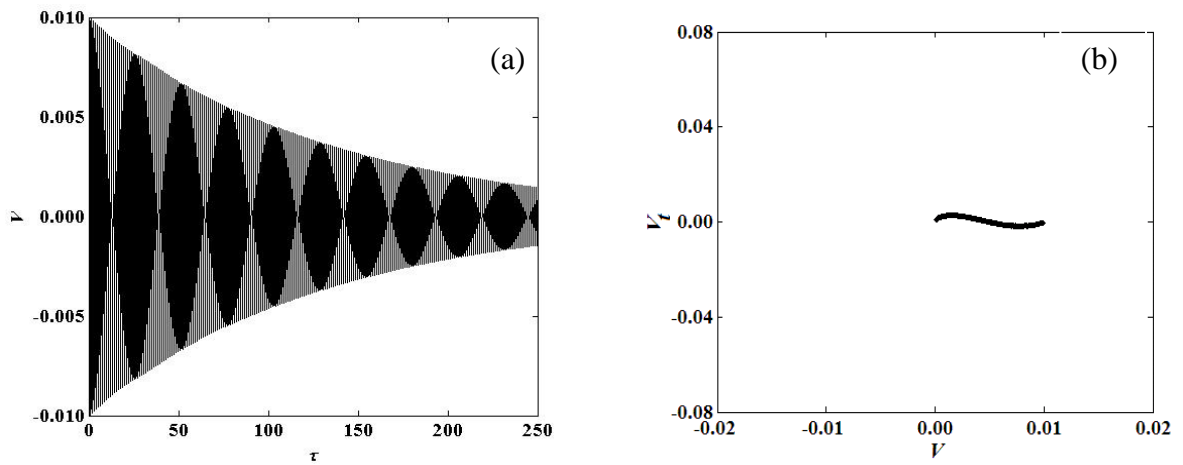**Fig.4.27:** Time history and Poincare's section at a spin speed Ω = 0 rad/s for c= 0.

Fig.4.28: Time history and Poincare's section at a spin speed Ω = 0 Hz for c = 0.05 Ns/m,
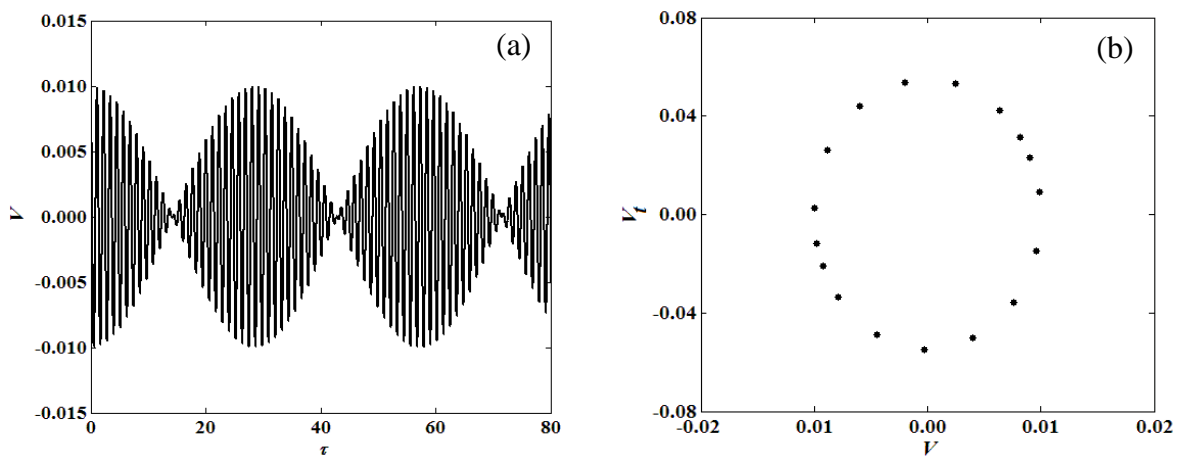

Fig.4.29: Time history and Poincare's section at a spin speed Ω = 10 Hz for c = 0.0 Ns/m
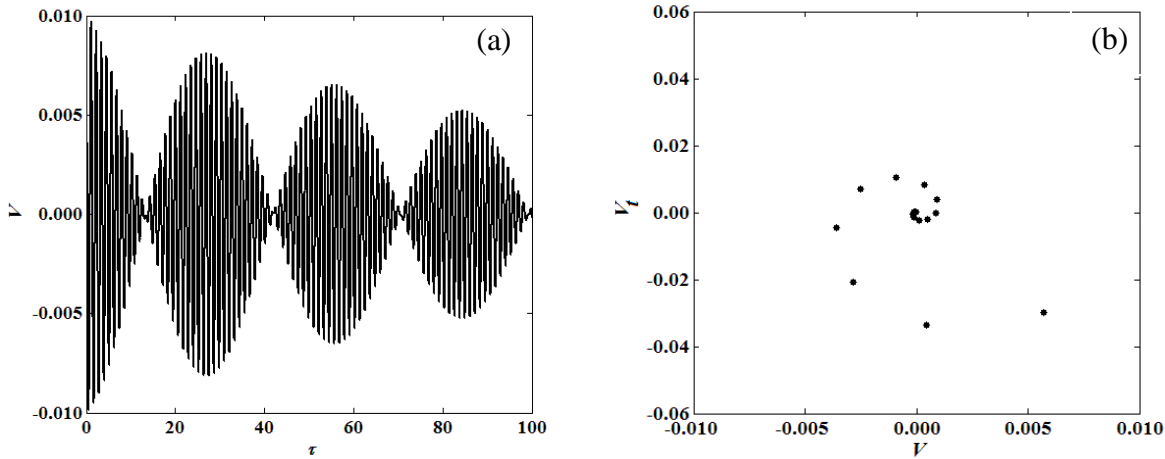
Fig.4.30: Time history and Poincare's section at a spin speed $\Omega = 10$ *Hz* for c = 0.05 *Ns/m*.

4.4 Excitation of geometric eccentricity and extra added mass (Phadatare et al., 2019)

Mechanical system with unbalance, especially in rotating machineries has been found to be one of the most common sources of mechanical vibrations which are further most susceptible to catastrophic structural failure. This unbalance may introduce at a manufacturing level or due to wear after long-run. Negligence of this unbalance in the system beyond an acceptable limit may result in poor outcome as well as may endanger surrounding environment and human life also. Thus, the present study considers the unbalance as a source of geometric eccentricity of the shaft-disk indicating an error at a manufacturing level and mass unbalance as an error due to wear along with the effect of nonlinearity in the shaft and bearing sections.

4.4.1 Analysis

A mathematical formulation is developed in this section to investigate the bifurcation and subsequent stability analysis of a light-weight rotor-disk-bearing framework subjected to amass unbalance and geometric eccentricity due to one of the manufacturing malfunctions. Here, the nonlinear flexible bearings are considered for the support of the rotating system.
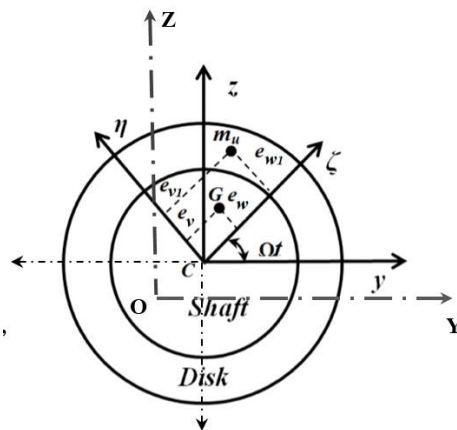

Fig.4.31 Conceptual model for unbalance and eccentricity

Figure 4.31 describes an external unbalance (m_u) and eccentricity of the rotor. The geometric eccentricity has been incorporated by taking into account the eccentricity e_v and e_w in the rotating plane along ζ and η directions, respectively. Moreover, a location of the unbalance mass is also been described with e_{v1} and e_{w1} in the same coordinated system. Relation between the location of the unbalance mass and the eccentricity can be described as $e_1 = e_{v1} - e_v$ and $e_2 = e_{w1} -$

82

e_w. The kinetic energy of the unbalance due to both the eccentricity of the rotor and the externally added unbalance mass (m_u) can be expressed as.

$$T_d = \Omega\left\{me_v\left(w_t\, c - v_t\, s\right) + Me_v\left(w_t\, c - v_t\, s\right)\big|_{x=Ld} + m_u e_{v1}\left(w_t\, c - v_t\, s\right)\big|_{x=L_d}\right\}$$
$$-\Omega\left\{me_w\left(v_t\, c + w_t\, s\right) + Me_w\left(v_t\, c + w_t\, s\right)\big|_{x=Ld} + m_u e_{w1}\left(v_t\, c + w_t\, s\right)\big|_{x=L_d}\right\}. \tag{4.22}$$

Here, c and s stand for $cos(\Omega t)$ and $sin(\Omega t)$, respectively.

Fig.3.4 displays a spring-damper model to represent the flexible bearings. The following additional non-dimensional terms are being used for the further analysis.

$$e_v^* = \frac{e_v}{L}, \quad e_w^* = \frac{e_w}{L}, \quad e_{v1}^* = \frac{e_v}{L}, \quad e_{w1}^* = \frac{e_w}{L}\, K_l^* = K_l L^4/D_{22}, \quad K_{nl}^* = 2K_{n1}L^6/D_{22},$$
$$c_b^* = c_b L^2/\sqrt{mD_{22}}. \tag{4.23}$$

Using the single mode Galerkin's approach, the partial differential equations of motion is discretized into temporal equations of motion by using following eigen function $\varphi(x)$ which has been obtained by considering the flexible bearings support.

$$\varphi(x) = \frac{\begin{array}{l}\left(\lambda^3\cos(\lambda) - \lambda^3\cosh(\lambda) + 2\sinh(\lambda)K_l\right)\left\{\sin(\lambda x) + \sinh(\lambda x)\right\} + \\ \lambda^3\left\{\sinh(\lambda) - \sin(\lambda)\right\}\left(\cos(\lambda x) + \cosh(\lambda x)\right)\end{array}}{\lambda^3\cos(\lambda) - \lambda^3\cosh(\lambda) + 2K_l\sin(\lambda)}. \tag{4.24}$$

Associated boundary conditions:

At $x = 0$, $\quad v_{xx} = 0, \quad v_{xxx} = -(K_l v_0 + cv_{0t}), \quad w_{xx} = 0, \quad w_{xxx} = -(K_l w_0 + cw_{0t}).$

At $x = L$, $\quad v_{xx} = 0, \quad v_{xxx} = K_l v_0 + cv_{0t}, \quad w_{xx} = 0, \quad w_{xxx} = K_l w_0 + cw_{0t}. \tag{4.25}$

The asterisk is dropped for simplicity. This eigen-function satisfies the above boundary conditions (a set of algebraic equations). The general equation of motion (i.e., Eqs. (4.9) and (4.10)) of the system can be re-written to include the effect of the unbalance mass and the eccentricity (Eq (4.22)). Substituting $\varphi(x)$ into the governing equations of the system, it results into the following equations.

$$\kappa_1 R_{tt} + c\kappa_2 R_t + \kappa_3 R - 2\Omega\kappa_4 S_t + \kappa_5(R^3 + RS^2) + \kappa_6 R^3 + \kappa_7(RR_t^2 + RS_t^2 + R^2 R_{tt} + RSS_{tt})$$
$$-\left(i\Lambda_2\Omega^2/2\right)\left\{e^{i\Omega t} - e^{-i\Omega t}\right\} + \left(\Lambda_1\Omega^2/2\right)\left\{e^{i\Omega t} + e^{-i\Omega t}\right\} = 0. \tag{4.26}$$

$$\kappa_1 S_{tt} + c\kappa_2 S_t + \kappa_3 S + 2\Omega\kappa_4 R_t + \kappa_5(S^3 + R^2 S) + \kappa_6 S^3 + \kappa_7(SR_t^2 + SS_t^2 + RS\ddot{R}_{tt} + S^2 S_{tt})$$
$$+\left(\Lambda_2\Omega^2/2\right)\left\{e^{i\Omega t} + e^{-i\Omega t}\right\} - \left(i\Lambda_1\Omega^2/2\right)\left\{e^{i\Omega t} - e^{-i\Omega t}\right\} = 0. \tag{4.27}$$

Where

$$\kappa_1 = \int_0^1\left(\varphi^2 - \varphi\varphi'' I_2 + \varphi_{x=L_d}^2\beta_1 - \varphi_{x=L_d}\left(\varphi''\right)_{x=L_d} I_{2d}\right)dx, \quad \kappa_2 = \int_0^1\left(\varphi^2 + \varphi_{x=0}^2 + \varphi_{x=L}^2\right)dx,$$

$$\kappa_3 = \int_0^1\left(\varphi\varphi'''' + \varphi_{x=0}^2 K_l + \varphi_{x=L}^2 K_l\right)dx, \quad \kappa_4 = -\int_0^1\left(\varphi\varphi'' I_2 + \varphi_{x=L_d}\left(\varphi''\right)_{x=L_d} I_{2d}\right)dx,$$

$$\kappa_5 = \int_0^1\left(\varphi\varphi'^2\varphi'''' + \varphi\varphi''^3 + 4\varphi\varphi'\varphi''\varphi'''\right)dx, \quad \kappa_6 = \int_0^1\left(\left(\varphi^4\right)_{x=0}K_{nl} + \left(\varphi^4\right)_{x=l}K_{nl}\right)dx,$$

$$\kappa_7 = \int_0^1\left(\varphi\varphi''\int_1^x\int_0^x\varphi'^2 dx dx + \beta_1\left(\varphi\varphi''\int_1^x\int_0^x\varphi'^2 dx dx\right)_{x=L_d} - \left(\varphi\varphi'\int_0^x\varphi'^2 dx + \beta_1\left(\varphi\varphi'\int_0^x\varphi'^2 dx\right)_{x=L_d}\right)\right)dx, \tag{4.28}$$

$$c = \int_0^1\left(\varphi^2 + \varphi_{x=0}^2 c_b + \varphi_{x=L}^2 c_b\right)dx, \quad \Lambda_1 = e_v + \left(\beta_1\, e_v + \beta_2(e_v + e_{v1})\right)\big|_{x=L_d},$$

$$\Lambda_2 = e_w + \left(\beta_1\, e_w + \beta_2(e_w + e_{w1})\right)\big|_{x=L_d}.$$

The above non-dimensional governing equations have forcing terms ($\Lambda_2\Omega^2\, sin\,\Omega t - \Lambda_1\Omega^2\, cos\,\Omega t\,/\Lambda_2\Omega^2\, cos\,\Omega t + \Lambda_1\Omega^2\, sin\,\Omega t$) in the planes x-z and x-y, respectively, along with other nonlinear terms. Since the governing equation of motion contains the nonlinear terms, the exact solutions are not available as obtaining closed form is somehow difficult. Therefore, one may go for an approximate solution by using the perturbation approach. Similar treatment as

described the previous chapter is carried out for the above equations of motion. Then, it results into following equations for order 1 of ε

$$\kappa_1 D_0^2 R_3 + \kappa_3 R_3 - 2\Omega\kappa_4 D_0 S_3 = -2\kappa_1 D_0 D_2 R_1 - \kappa_2 c D_0 R_1 + 2\kappa_4 \Omega D_2 S_1 - (\kappa_5 + \kappa_6) R_1^3$$
$$- \kappa_5 R_1 S_1^2 - 2\kappa_7 (D_0^2 R_1^3 + D_0^2 R_1 S_1^2) - \tag{4.29}$$
$$\frac{1}{2}\Omega^2 \Lambda_1 (e^{i\Omega T_0} + e^{-i\Omega T_0}) - \frac{1}{2}i\Omega^2 \Lambda_2 (e^{i\Omega T_0} - e^{-i\Omega T_0}).$$

$$\kappa_1 D_0^2 S_3 + \kappa_3 S_3 + 2\Omega\kappa_4 D_0 R_3 = -2\kappa_1 D_0 D_2 S_1 - \kappa_2 c D_0 S_1 - 2\kappa_4 \Omega D_2 R_1 - (\kappa_5 + \kappa_6) S_1^3$$
$$- \kappa_5 S_1 R_1^2 - 2\kappa_7 (D_0^2 S_1^3 + D_0^2 S_1 R_1^2) - \tag{4.30}$$
$$\frac{1}{2}i\Omega^2 \Lambda_1 (e^{i\Omega T_0} - e^{-i\Omega T_0}) + \frac{1}{2}\Omega^2 \Lambda_2 (e^{i\Omega T_0} + e^{-i\Omega T_0}).$$

It may be noted that these equations have secular or small divisor terms when the system is subjected to the primary resonance condition $\Omega \approx N_f$. Thus, by substituting $\Omega = N_f + \varepsilon^2 \sigma$ in Eqs.(4.29) and (4.30), The equations can be written as

$$\kappa_1 D_0^2 R_3 + \kappa_3 R_3 + 2\Omega\kappa_4 D_0 S_3 =$$

$$\left\{ \begin{array}{l} \left(-\frac{1}{2}N_f^2 \Lambda_1 - \frac{1}{2}iN_f^2 \Lambda_2\right)e^{i\sigma T_0} + 2i(\kappa_4\Omega - \kappa_1 N_f)D_2 F_1(T_2) - i\kappa_2 c N_f F_1(T_2) \\ -(4\kappa_5 + 3\kappa_6)F_1^2 \bar{F}_1 + (2\kappa_7 (N_f + N_b)^2 - 2(4\kappa_5 + 3\kappa_6))F_1 F_2 \bar{F}_2 \end{array} \right\}e^{N_f T_0 i}$$

$$+ \left\{ \begin{array}{l} 2i(\kappa_4\Omega + \kappa_1 N_b)D_2 F_2(T_2) - i\kappa_2 c N_b F_2(T_2) - (4\kappa_5 + 3\kappa_6)F_2^2 \bar{F}_2 \\ +(2\kappa_7 (N_f + N_b)^2 - 2(4\kappa_5 + 3\kappa_6))F_1 F_2 \bar{F}_1 \end{array} \right\}e^{N_b T_0 i} + CC + NST. \tag{4.31}$$

$$\kappa_1 D_0^2 S_3 + \kappa_3 S_3 - 2\Omega\kappa_4 D_0 R_3 =$$

$$\left\{ \begin{array}{l} \left(\frac{1}{2}N_f^2 \Lambda_2 - \frac{1}{2}iN_f^2 \Lambda_1\right)e^{i\sigma T_0} + 2(\kappa_4\Omega - \kappa_1 N_f)D_2 F_1(T_2) - \kappa_2 c N_f F_1(T_2) \\ +i(4\kappa_5 + 3\kappa_6)F_1^2 \bar{F}_1 - i(2(\kappa_7 + \kappa_{7d})(N_f + N_b)^2 - 2(4\kappa_5 + 3\kappa_6))F_1 F_2 \bar{F}_2 \end{array} \right\}e^{N_f T_0 i}$$

$$+ \left\{ \begin{array}{l} 2(\kappa_4\Omega + \kappa_1 N_b)D_2 F_2(T_2) - \kappa_2 c N_b F_2(T_2) - i(4\kappa_5 + 3\kappa_6)F_2^2 \bar{F}_2 + \\ i(2\kappa_7 (N_f + N_b)^2 - 2(4\kappa_5 + 3\kappa_6))F_1 F_2 \bar{F}_1 \end{array} \right\}e^{N_b T_0 i} + CC + NST. \tag{4.32}$$

The above Eqs.(4.31) and (4.32) are composed of secular or small divisor terms. As a result, solutions of these equations can be unbounded. Therefore, satisfaction of the solvability conditions is necessary to analyze the bounded steady state solutions of the system. Therefore, the solvability conditions can be written as.

$$2i(\kappa_4\Omega - \kappa_1 N_f)D_2 F_1(T_2) - i\kappa_2 c N_f F_1(T_2) - (4\kappa_5 + 3\kappa_6)F_1^2 \bar{F}_1 +$$
$$(2\kappa_7 (N_f + N_b)^2 - 2(4\kappa_5 + 3\kappa_6))F_1 F_2 \bar{F}_2 - N_f^2 (\Lambda_1 / 2 + i\Lambda_2 / 2)e^{i\sigma T_0} = 0. \tag{4.33}$$

$$2i(\kappa_4\Omega - \kappa_1 N_b)D_2 F_2(T_2) - i\kappa_2 c N_b F_2(T_2) - (4\kappa_5 + 3\kappa_6)F_2^2 \bar{F}_2 + (2\kappa_7 (N_f + N_b)^2$$
$$-2(4\kappa_5 + 3\kappa_6))F_2 F_1 \bar{F}_1 = 0. \tag{4.34}$$

The term F_1 and F_2 can be expressed in the forms as $(1/2)d_1 e^{i\theta_1}$ and $(1/2)d_2 e^{i\theta_2}$, respectively and substituting it into Eqs.(4.33) and (4.34). Then, the resulting equations can be manipulated to obtain following expressions by separating the real and imaginary terms as.

$$d_1 \frac{\partial \theta_1}{\partial T_2} = \frac{\left\{(2\kappa_5 + 3\kappa_6 / 2)d_1^3 + \left\{(4\kappa_5 + 3\kappa_6) - \kappa_7 (N_f + N_b)^2\right\}d_1 d_2^2 + 2\Lambda_1 N_f^2 \sin\gamma\right\}}{4(\kappa_4\Omega - \kappa_1 N_f)}. \tag{4.35}$$

$$\frac{\partial d_1}{\partial T_2} = \left\{-\kappa_2 c N_f d_1 + \Lambda_1 N_f^2 \cos\gamma\right\} / 2\left\{\kappa_4\Omega - \kappa_1 N_f\right\}. \tag{4.36}$$

$$\frac{\partial \gamma}{\partial T_2} = \sigma - \frac{\partial \theta_1}{\partial T_2}. \tag{4.37}$$

We use $d_1' = \gamma' = 0$ in Eqs.(4.35)- **Error! Reference source not found.** to obtain the steady-state solution near primary resonance condition. The resultant nonlinear algebraic equations can

be numerically solved to understand the nonlinear response of the system under effect of the change in values of the system parameters.

4.4.2 Result and Discussion

Physical and geometric properties of the rotor-bearing system are hereby taken as: shaft length ($L = 1m$), disk position ($L_d = L/3$), geometric eccentricity ($e_w = e_w = 1.25 \times 10^{-4} m$), the unbalance mass location ($e_{v1} = e_{w1} = 49.64 \times 10^{-3}$ m), disk radius ($R_d = 0.07m$), non-dimensional disk mass ($\beta_1 = 1.5$), diametrical moment of inertia ($I_3 = 6.25 \times 10^{-4}$), and an unbalance mass ($\beta_2 = 3.7 \times 10^{-3}$).
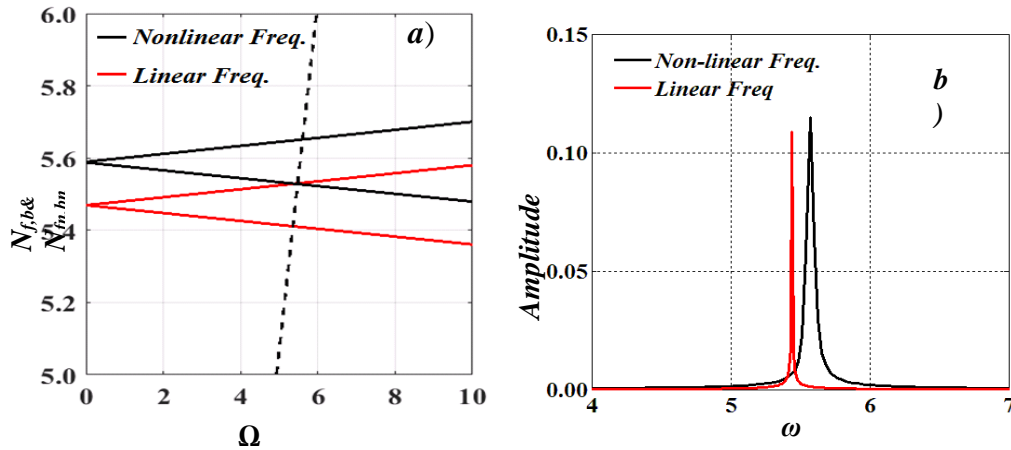
Fig.4.32: a) Campbell diagram b) FFT plot of intial $3sec$ data at $\Omega = 0$ Hz : $v(0) = 0.15$, $w(0) = 0.00$

Theoretical studies have been carried out to explore the stability, bifurcation and critical operating conditions for the primary resonance case when the destabilized parameters such as geometric eccentricity, disk position, disk mass, an unbalance mass and its moment of inertia have been. These observations have been demonstrated using simulation tools such as the frequency response curves, time responses, Fourier spectrums, Phase-space plot and Poincare's map to understand the vibration characteristics and stability of the system. Simultaneously, the Campbell diagram and FFT have been developed for obtaining the natural frequencies for both the linear and nonlinear models of the rotating system shown in Fig.4.32, while the comparison between linear and nonlinear frequencies has been well verified in Fig.4.32b for a certain speed. It has been found that the nonlinear frequencies come up about 5-6% higher as compared with the linear ones.
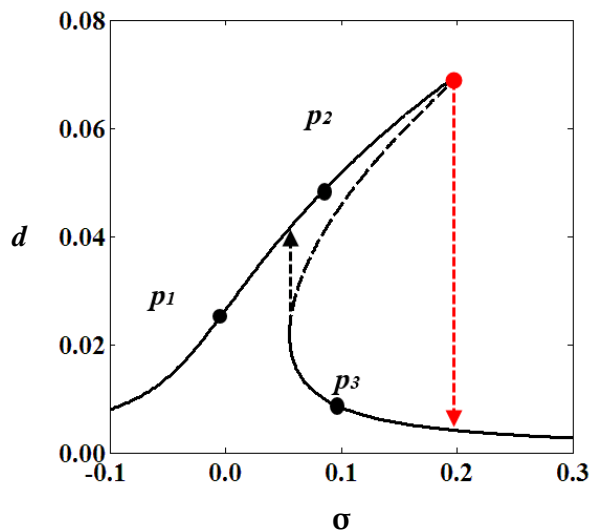

Fig.4.33: Frequency response plot

Typical frequency response curves indicating how the vibration amplitude gets changed with the external frequency of mass unbalance have been depicted for primary resonance

condition. Here, the solid and dotted lines indicated the stable and unstable solutions, respectively. Since the system does not impart any trivial solution ($d_1=0$), the rotating shaft vibrates with an amplitude equal to that of non-trivial ($d_1\neq0$) as shown in Fig. 4.33. For an upward sweep, the flexible shaft disk system expriences a jump down phenomenon (as depicted by dotted red line) for a slight increase in frequency of the mass unbalance at a critical pont which is known as S-N bifurcation. As a result, a sudden decrease in the amplitude is being observed that lead to a catastrophic failure due to the repeated occurrences. For a downward sweep, the jump up phenomena occurs when a slight decrease in frequency at a point, also known as S-N bifurcation takes place. Thus, here also the system leads to a catastrophic failure because of sudden jump in the response. The initial conditions may act an important role to perceive the actual geometry of the motion for its bi-stability. Figure 4.33 shows results obtained using the approximation technique that have been verified by numerically solving Eqs.(4.35)-**Error! Reference source not found.**keeping the parameters value same for the three points, marked as P_1, P_2, and P_3 in the frequency response curve. For these initial excitations, the corresponding time responses, phase portraits, FFTs and Poincare's sections have been diagrammed in Fig.4.34.
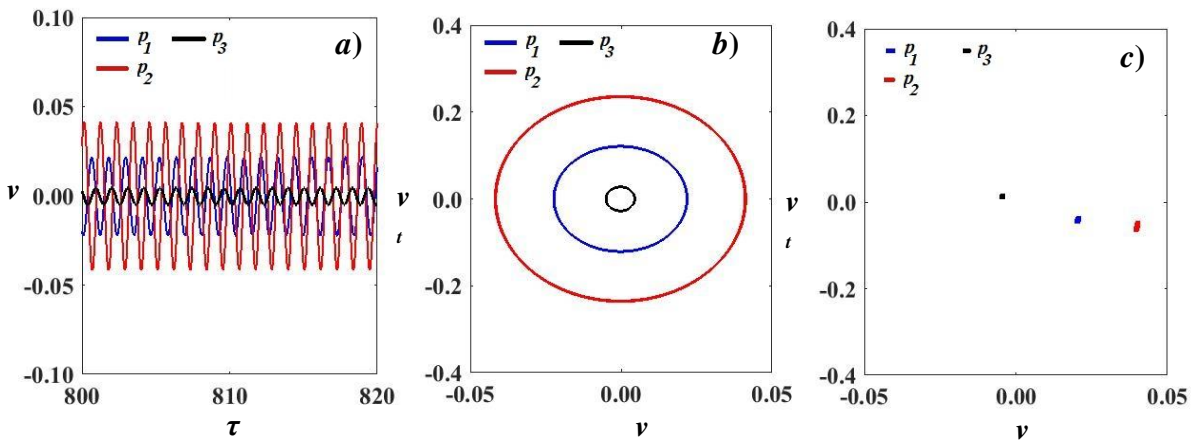
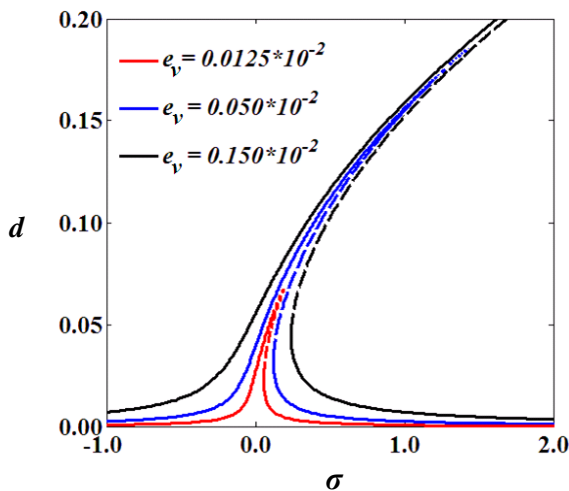**Fig.4.34:** Steady state response only (Ref. Fig4.33) a) Time response b) Phase portrait c) Poincare map

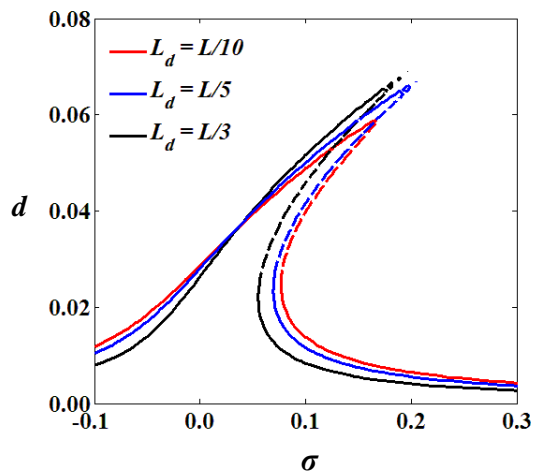**Fig.4.35:** Frequency response curve for Different eccentricity ($e_v = e_w$).

Fig.4.36: Frequency response curve for different disk position (L_d)

. It has been depicted that the both results are in accordance and show mostly the periodic behaviour for any steady state response. The response amplitude is found to be the 3-5% error with the magnitude reported in the frequency response curves. Moreover, the steady state response is fully dominated by the forcing term at these points. Figure 4.35 describes the effect of

eccentricity on the dynamic responses. It has been observed that the response amplitude increases with increase in the eccentricity. As a result, the region where the system losses its stability gets increased. Thus, by selecting an appropriate value of the eccentricity, the behaviour of the system can be effectively controlled as well as catastrophic failure may be avoided subsequently. Figure 4.36 shows effect of positioning of the disk on the nonlinear behaviour of the rotor. It has been observed that vibration amplitude gets significantly reduced tending hardening effect when the disk is located away from a mid-point of the shaft. Hence, it can be said that with increase in the shaft speed causes the sharp increase in the vibration amplitude when the disk is located away from mid-span of the shaft.
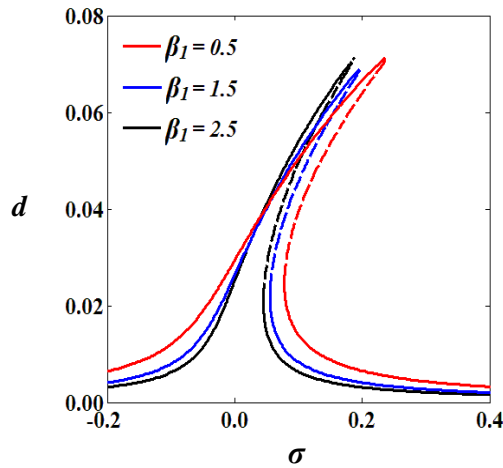
Fig.4.37: Frequency response curve for different disk mass (β_1)
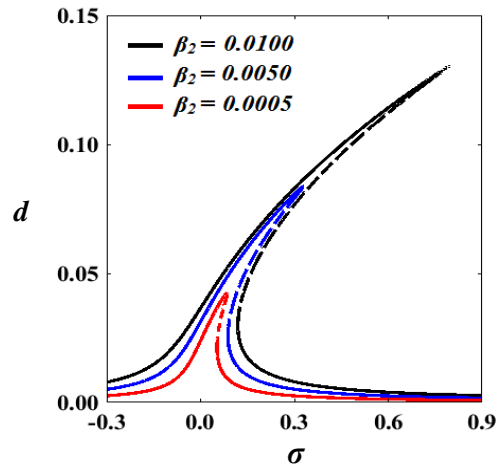
Fig.4.38: Frequency response curve for different unbalance (β_2) : β_1=0.5.
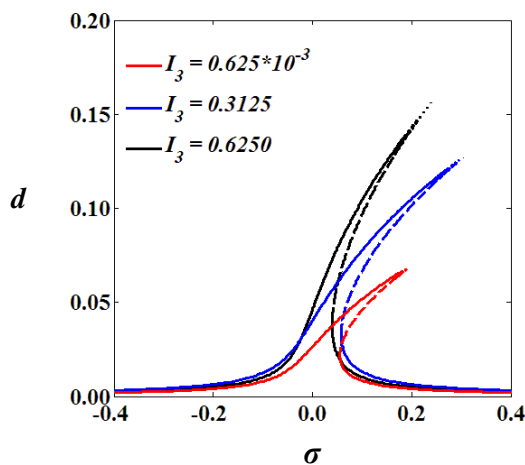
Fig.4.39: Frequency response curve for different diametrical moment of inertia (I_3)
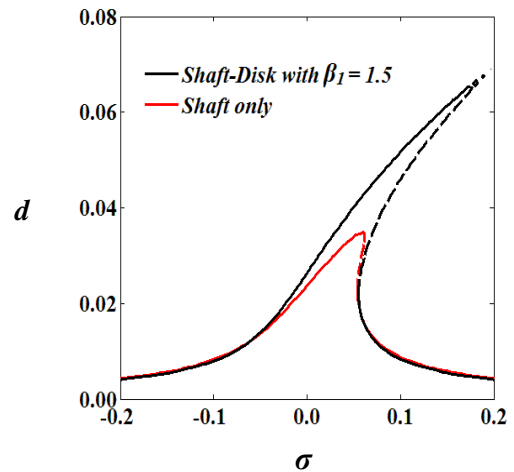

Fig.4.40: Frequency response curve for the rotating system with and without disk (same unbalance magnitude ($\beta_2 e_{v_1}$) for both cases)

A change in mass of the disk also causes variation in the nonlinear behaviour of the system. This has been depicted in Fig.4.37. For a moderately large value of the disk-mass, the region of instability improves into the smaller range. However, the maximum amplitude of vibration is not observed to be affected with the change in the disk-mass. Figure 4.38 portrays the effect of the extra added unbalance mass (β_2) on the bifurcation and system's stability. Here, three values of the unbalance mass (β_2) such as 0.01, 0.005 and 0.0005 are considered for this analysis. These different values of β_2 exhibit prominent effect on the amplitude and the instability range of the system. It is observed that the amplitude and the instability range become smaller when the value of the unbalance mass (β_2) becomes reasonably small.

It is observed that the vibration amplitude gets increased with increase in the mass moment of inertia (I_3) of the disk since the overall rotational inertia gets higher with increase in the I_3 as depicted in Fig.4.39. In addition, the system shows decrease in the hardening effect with increase in the I_3. Consequently, the system has a smaller region of the instability for a higher value of the I_3. Figure 4.40 demonstrates the frequency response curves of the rotating system with and without a disk. Here, same magnitude of the unbalance mass (β_2) is considered for both these cases. As expected, the vibration amplitude is found to be higher for a system with the disk as compared to the system without the disk. This is because of higher effective rotational inertia for the system with the disk. For a specific value of the β_2, the response of the shaft may observe to be approximately linear in nature as the region of instability disappears from the response curves. Hence, the stability of the shaft element is merely affected with the nonlinearity.
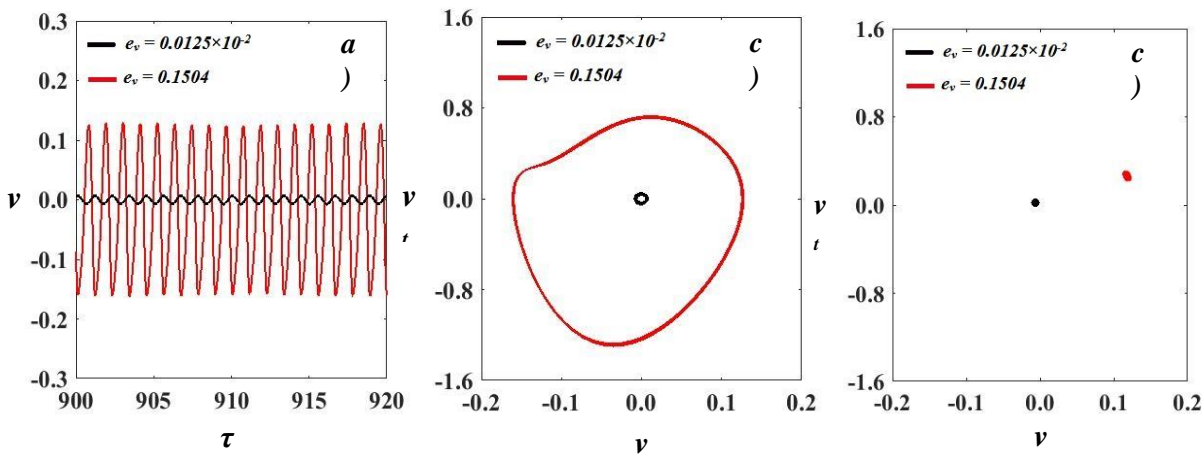

Fig.4.41: Steady state response only. a) Time response b) Phase portrait c) Poincare map. : $v(0) = 0.01$, $e_v = e_w, e_{v1} = e_{w1} = 0.2374$.
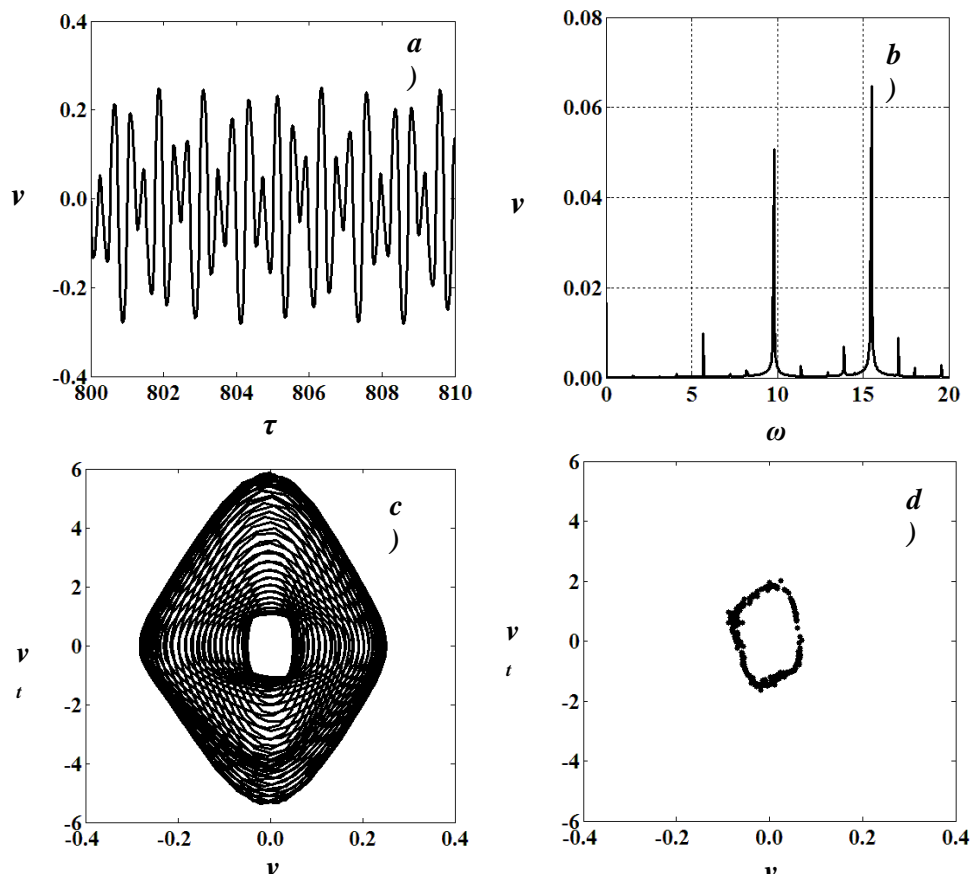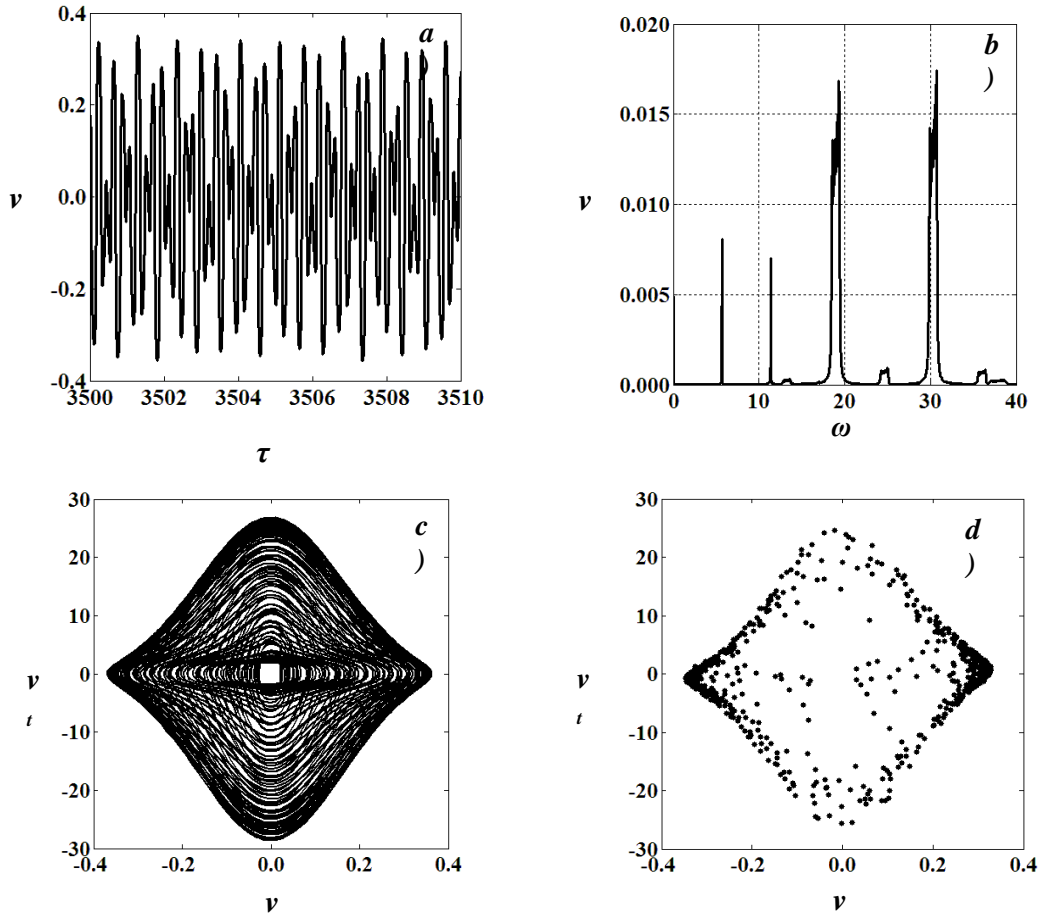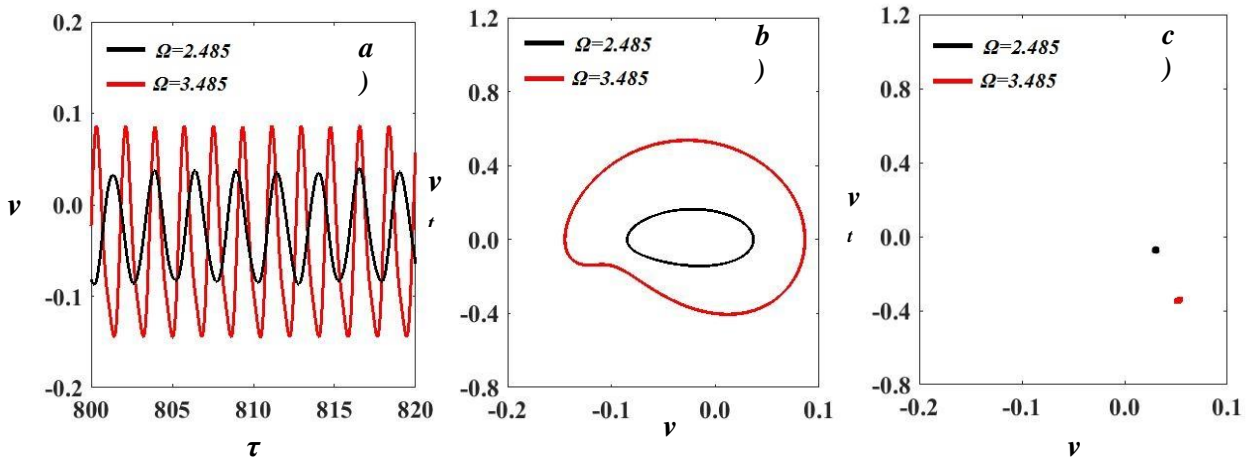

Fig.4.42: Steady state response only. a) Time response b) FFT plot c) Phase portrait d) Poincare map. : $v(0) = 0.01$, $e_v = e_w = 0.1880$, $e_{v1} = e_{w1} = 0.2374$

88

Fig.4.43: Steady state response only. a) Time response b) FFT plot c) Phase portrait d) Poincare map. : $v(0) = 0.01$, $e_v = e_w = 0.2505$, $e_{v1} = e_{w1} = 0.30$

The diagnosis and forecast of the chaotic behaviour, i.e., a route to chaos upon changing the control parameters has been studied with the demonstration of time history, phase portraits, Fourier spectrum, Poincare's map and bifurcation diagrams. Here, the presence of chaotic responses has been investigated with the change in eccentricity in the rotating shaft-disk system as shown in Figs.4.41-4.43. The system exhibits a periodic behaviour with a perfect circular trajectory projected in the phase planes and a point in the Poincare's section when the eccentricity becomes small i.e., $e_v = e_w = 1.25 \times 10^{-4}$. With increase in the eccentricity value to $e_v = e_w = 1.504 \times 10^{-1}$, an irregular closed shape with a small peak of frequencies other than the dominant frequency can be observed. With further increase in the eccentricity value to 0.1880, the system has dominant of more than one frequency and exhibits beating phenomenon leading to a quasi-periodic behaviour shown in Fig.4.42. Finally, the systems undergoes chaotic behaviour when the eccentricity becomes $e_v = e_w = 0.2505$ that has been clearly observed in FFT, Poincare's section and phase planes with multidimensional torus type shape shown in Fig.4.43. Hence, the rotor-disk system exhibits the chaotic behaviours when the geometric eccentricity crosses its critical value.

Figures 4.44–4.47 show the behaviour of the system due to rise in a spin speed of the rotor. It shows a periodic behaviour at $\Omega=2.485$, 3.485, respectively and a quasi-periodic behaviour when the spin speed rises to $\Omega=4.485$. The system undergoes chaotic behaviour with the sequences of period-doubling at $\Omega=5.485$, 5.685. Therefore, it can say that the change in the spin speed may cause changes in the vibration behavior of the system while at a high spin speed, the system reveals chaotic response. Hence, the system encounters the chaotic behaviour when the shaft speed passes through its critical value.
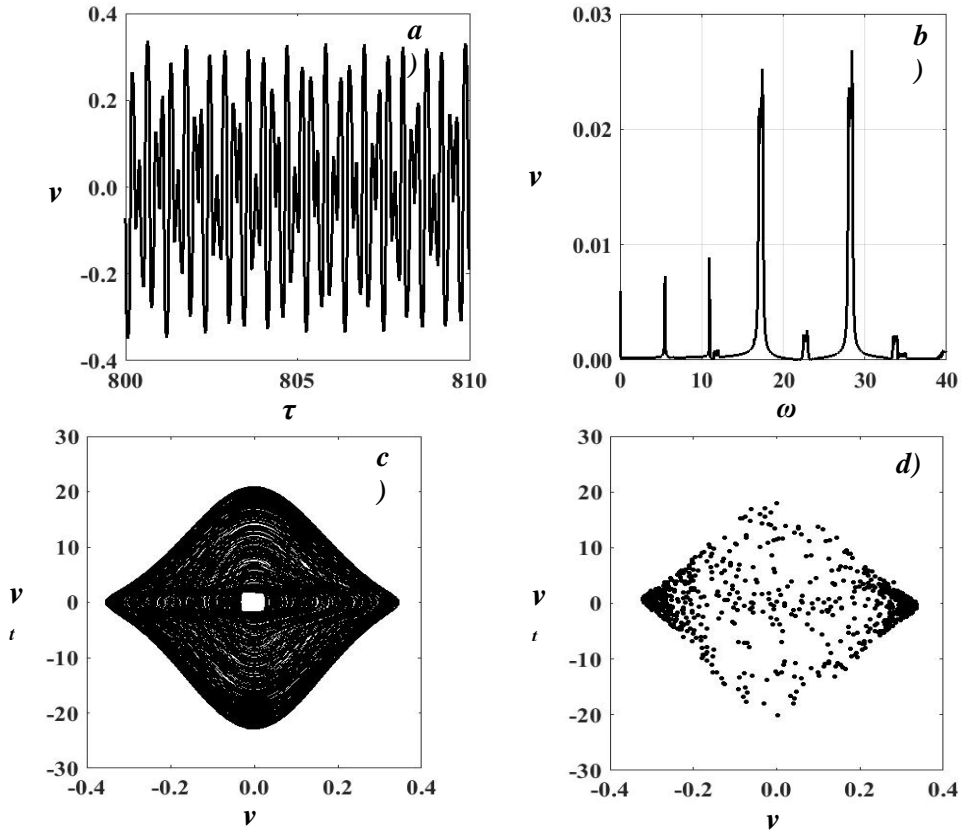
Fig.4.44: Steady state response only. a) Time response b) Phase portrait c) Poincare map. : $e_v = e_w = 0.125$
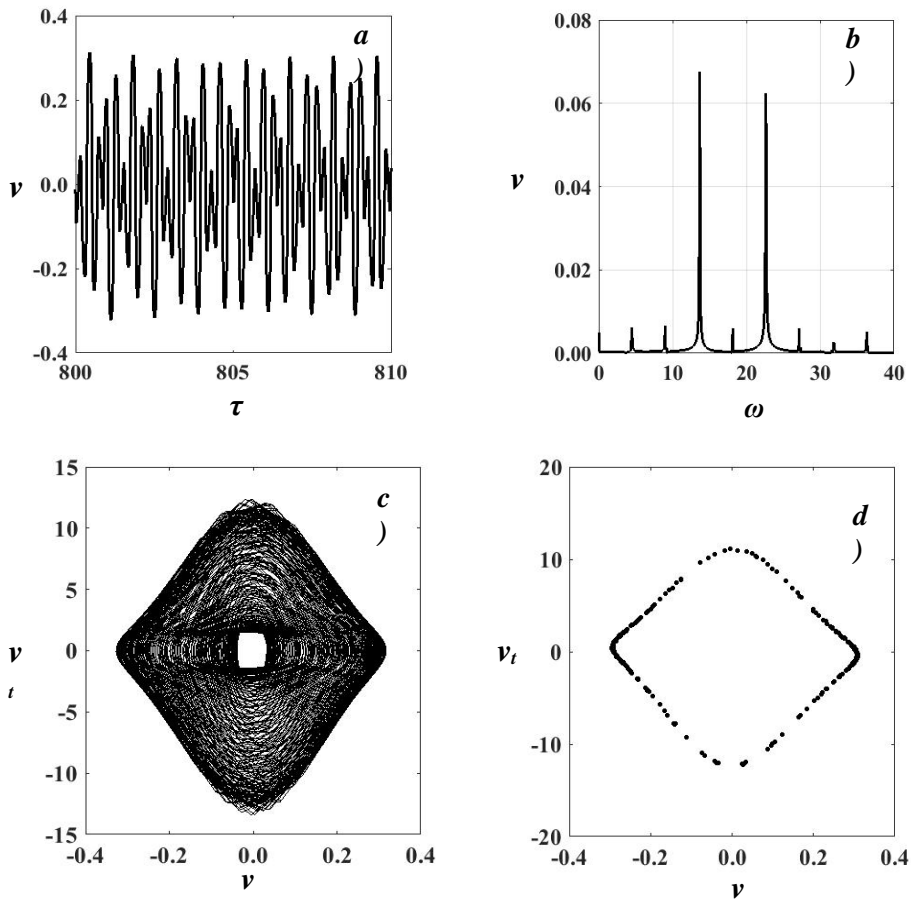

Fig.4.45: Steady state response only. a) Time response b) FFT plot c) Phase portrait c) Poincare map. : $e_v = e_w = 0.125$, $\Omega = 4.485$

The bifurcation diagrams to study the essential dynamics of the systems in order to identify the instabilities way forward to chaotic behaviours has been presented for the geometric eccentricity and the speed of the shaft as shown in Fig. 4.48. The overall system is found to be under control when the shaft speed is being kept either 4.285 or 10.29. In this range, the behaviour is observed to be either stable periodic or quasi-periodic. Similarly, the system leads to an unstable state when the value of the geometric eccentricity rests between range 0.0215 and 0.026 and shows the chaotic nature of vibration. For all the value of 0.026, the dynamic characteristics remain to be quasi-periodicity.

Fig.4.46: Steady state response only. a) Time response b) FFT plot c) Phase portrait d) Poincare map. : $e_v = e_w$= 0.125, Ω=5.485
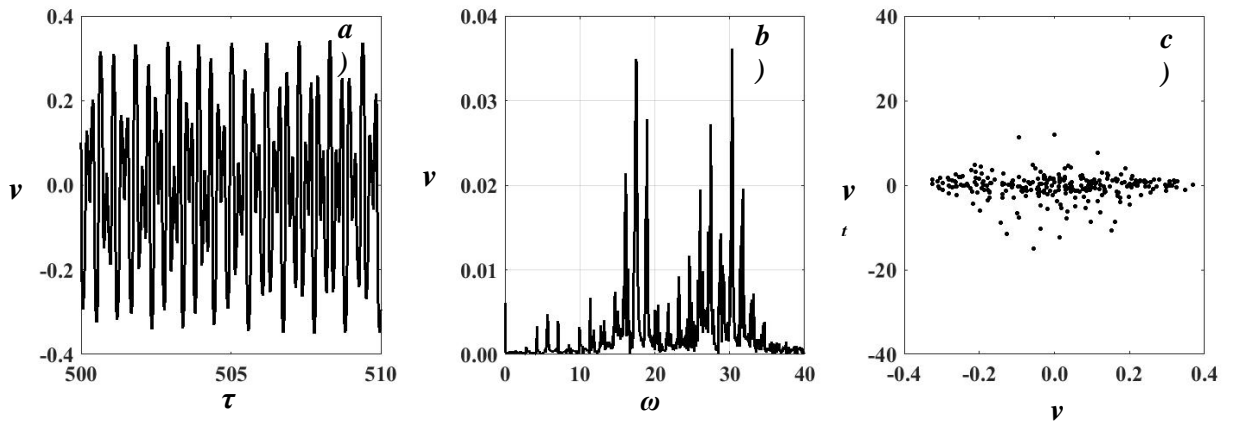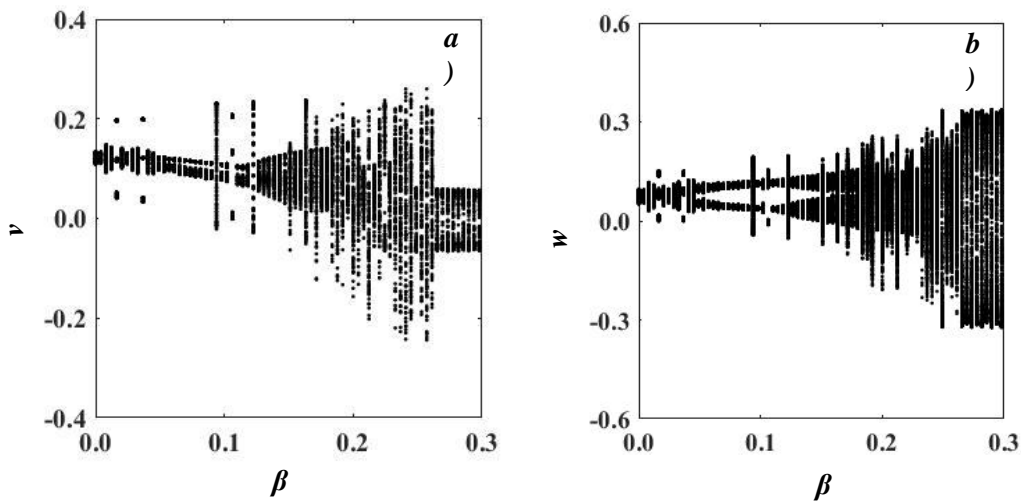

Fig.4.47: a) Time response b) FFT plot c) Poincare map. : $e_v = e_w$= 0.125, Ω=5.685

Figure 4.49 exhibits a bifurcation diagram with the mass unbalance as a control parameter using Poincare's maps. It shows that with increase in the mass unbalance initially appears static bifurcation. With further gradual increase in the mass unbalance, the system responses finally evolve to a chaotic behaviour with the possible consequences of quasi-periodic, period-doubling, sudden transitions, and intermittency routes. In Fig.4.49, the system behaviour against the change in β_2(range 0 to 0.3) with Ω=10 is portrayed. At β_2=0.004, the system shows a periodic motion while the periodic motion diverts to a double-periodic motion when the β_2 increases to 0.0069 in Fig.4.50. The system shows the chaotic response for any value of β_2 between 0.1837 and 0.2572. With further increase in the β_2 causes period-double phenomena and finally the system undergoes a chaotic behaviour for the β_2 equal to 0.28 as shown in Fig.4.51. Thus, the unbalance effect at a high speed condition influences the system behaviour substantially where the behaviour of the system changes from one form to another. Hence, with a proper selection of the
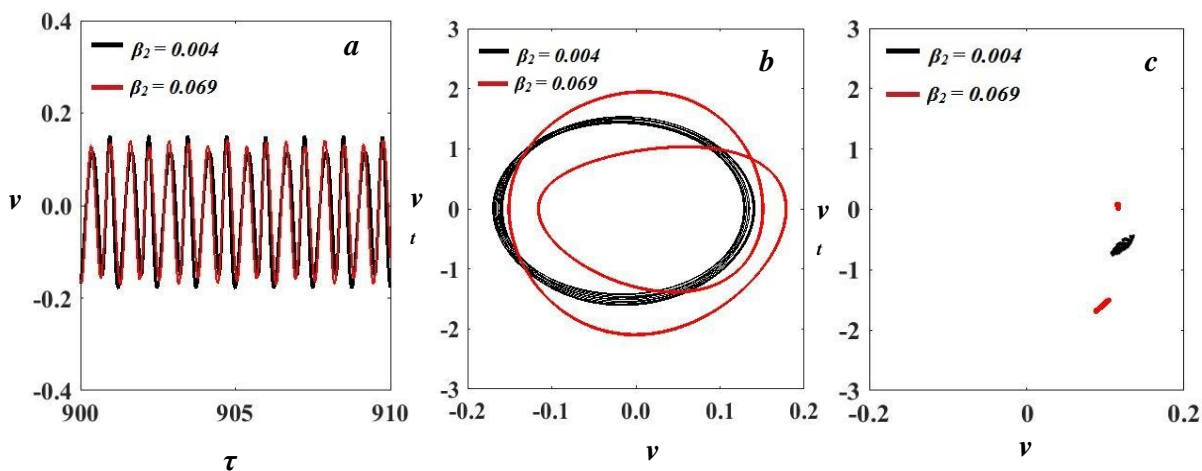
mass unbalance i.e., magnitude and location, a well-controlled behaviour of the system may achieve.
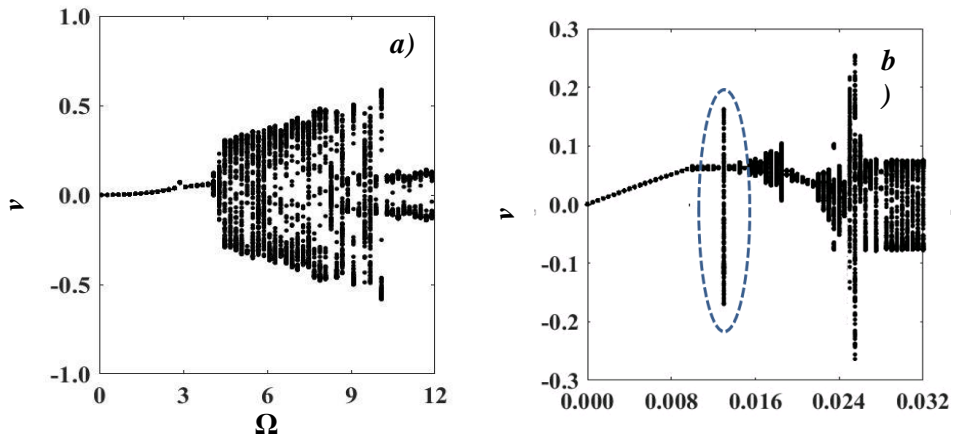
Fig.4.48: Bifurcation diagram a) Spin speed (Ω) Vs Poincare points (v) with ($v(0)$= 0.01) b) eccentricity (e_v) Vs Poincare points (v) with ($v(0)$= 0.01, $\mathcal{V}_t$ (0)= 0.02, w(0)=0.0001, $\mathcal{W}_t$ (0)=0.01)

Fig.4.49: Bifurcation diagram a) β_2 Vs Poincare points (v) b) β_2 Vs Poincare points (v) with ($v(0)$ = 0.001), $v_t(0)$= 0, w(0)=0, $w_t(0)$=0), e_v = e_w = 0.02

.

Fig.4.50: Steady state response only (Ref.Fig.4.49). a) Time response b) Phase portrait c) Poincare map
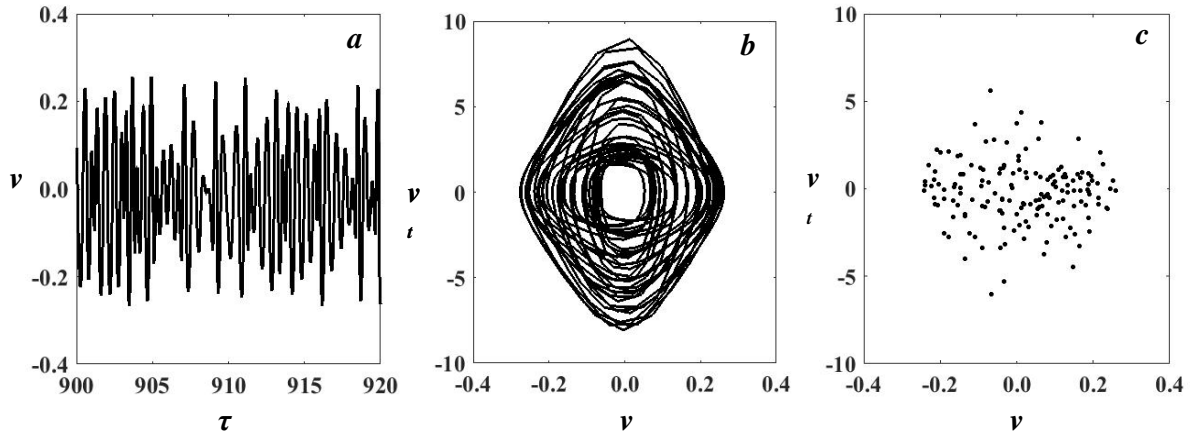
Fig.4.51: Steady state response only (Ref. Fig.4.49). a) Time response b) Phase portrait c) Poincare map. β_2= 0.28

We further depicted the frequency response curves for the system with and without the flexible bearing-supports in Fig.4.52, it has been observed that the flexible bearing gives rise to system stability by reducing the instability regions. Thus, the system has brought down to a stable state when the rotating shaft is mounted on the flexible bearings instead of the rigid one. The frequency response curves have been diagrammed to know the effect of nonlinear stiffness characteristics onto the system dynamics as shown in Fig.4.53. It has been observed that the system shows the hardening effect with nonlinear stiffness K_{nl}. Further, no substantial changes in the nonlinear responses are observed with the changes of the linear stiffness (K_l). It has been observed that the response amplitude decreases with increase in the K_{nl}. Thus, the vibration amplitude can be under control with the increase in the spring stiffness or can be brought down to a stable single solution with the increase in the spring stiffness. Hence, for a moderately large value of the spring stiffness, the system may behave same as that of linear one since the jump length is here found to be negligible. Hence, catastrophic failure due to the bifurcation can effectively be controlled with an appropriate selection of the spring value.
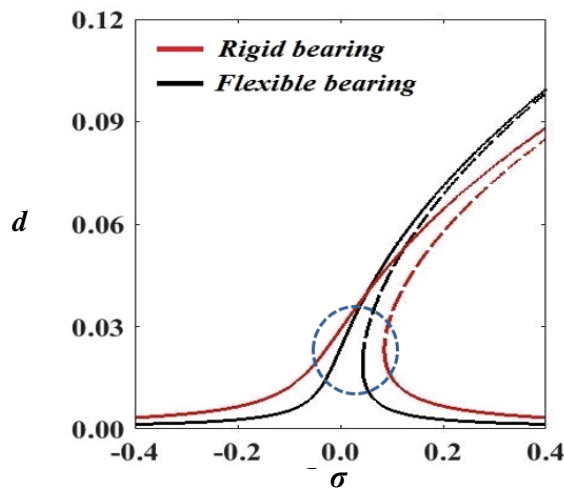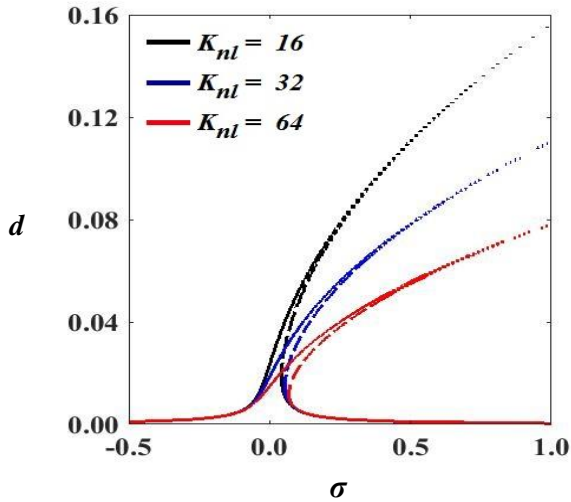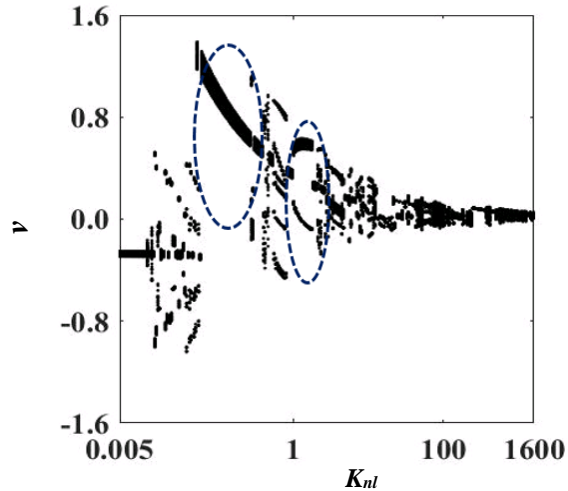

**Fig.4.52:** Frequency response curve: K_l =0.016, C_b=8.57×10^{-4}

Fig.4.53: Frequency response curve: K_l =0.016, C_b =8.57×10^{-4}

Fig.4.54: Bifurcation diagram   a) K_{nl}Vs Poincare points (v) with (v(0) = 0.001), $\dot{v}$(0)= 0, w(0)=0, $\dot{w}$(0)=0), β_2 = 0.018, $e_v = e_w$ = 0.02

Figure 4.54 shows bifurcation diagram for the nonlinear stiffness in the vertical direction within a range from 0.005 to 1600 with Ω=10. This diagram indicates significant behavioural changes within the system from a periodic to a chaotic. At K_{nl} =0.005, the system shows a periodic motion while a slight change in the value causes the period-doubling phenomenon. Finally, the system experiences N-periodic behaviour with further increases in the stiffness. The instantaneous transition from period-k motion to period-2k motion has been found with the gradual change in the stiffness value and eventually resulting into a chaos. This route to chaos behaviour has been also verified by portraying the time series, phase portrait and Poincare's map for the selected values K_{nl} as shown in Fig.4.55-4.56. With this observation, it can be concluded that the variation of K_{nl} can change the behaviour of the system from one form to another. Therefore, this parameter can be used as a control parameter in order to decide the future dynamic behaviour of the system.
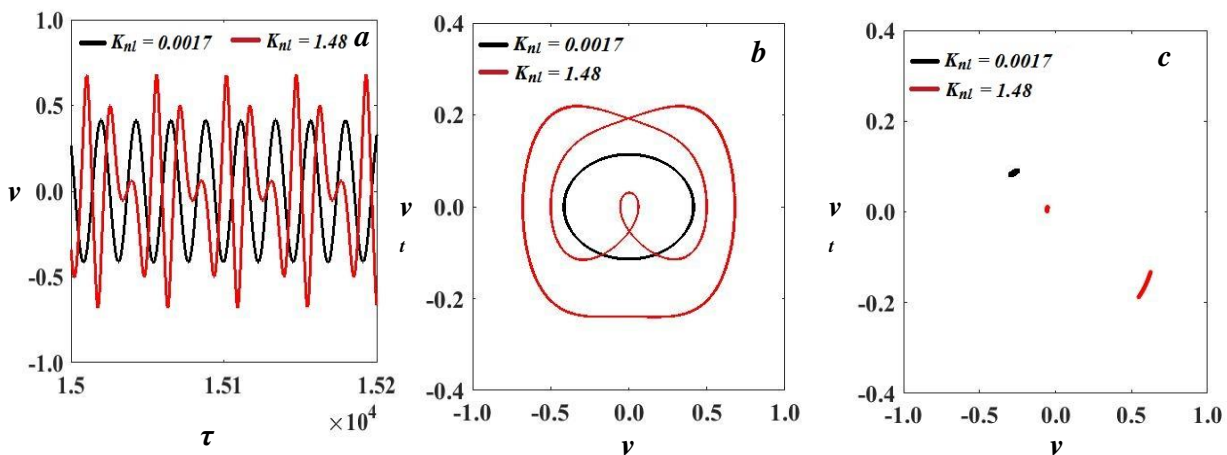
Fig.4.55: Steady state response only (Ref.4.54) a) Time response b) Phase portrait c) Poincare map
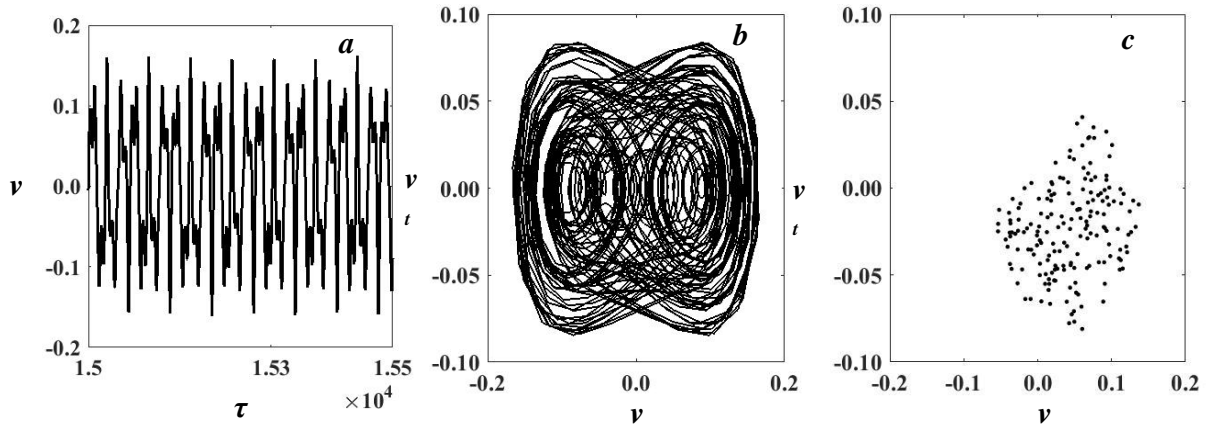
Fig.4.56: Steady state response only (Ref.4.54) a) Time response b) Phase portrait c) Poincare map $K_{nl} = 78$

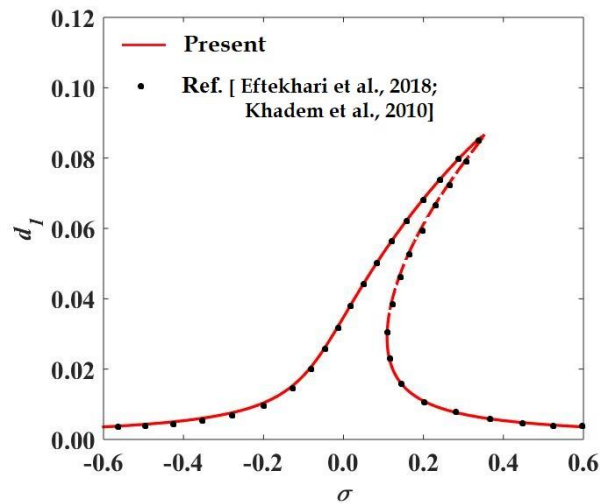**d.** *Validation of the present model with a published research*

Fig. 4.57: Validation: Frequency response plot

The frequency response plot (Fig. **4.57**) is portrayed by neglecting the extra unbalance term and effect of the bearings with considering the same configuration as Eftekhari et al. (2018) and Khadem et al. (2010). The solid red colour lines represent results from the proposed model and the black dotted lines represent results from the published articles. It has been found that the results of proposed models are in concurrence with the those presented by Eftekhari et al. (2018) and Khadem et al. (2010).

4.5   Excitation of an unbalance with rub impact phenomenon

This section is devoted to investigate the stator and disk interaction of a geometrically nonlinear rotor system with large deformation in the bending having rigid bearings support. This work is an extension of the rotating model of the previous section. The system is subjected to combined forces such as a force due to the presence of unbalance and forces developed due to rubbing between the stator and the rotating disk. The system is analyzed to understand the effects of variation in the stator stiffness, rotating speed, coefficient of friction and an unbalance mass for the proposed model of the rotating system.

95

4.5.1 Analysis

A rub impact shaft disk system with nonlinearity due to large deformation is considered as shown in Fig.4.58. The shaft is flexible with length L, radius R_s mass per unit length m, the disk is rigid (has outer radius R_d, mass M, thickness h) and mounted at a distance L_d from one end of the shaft

$$\text{So, } F_y = -F_N \cos\psi + F_T \sin\psi,$$
$$F_z = -F_N \sin\psi - F_T \cos\psi.$$
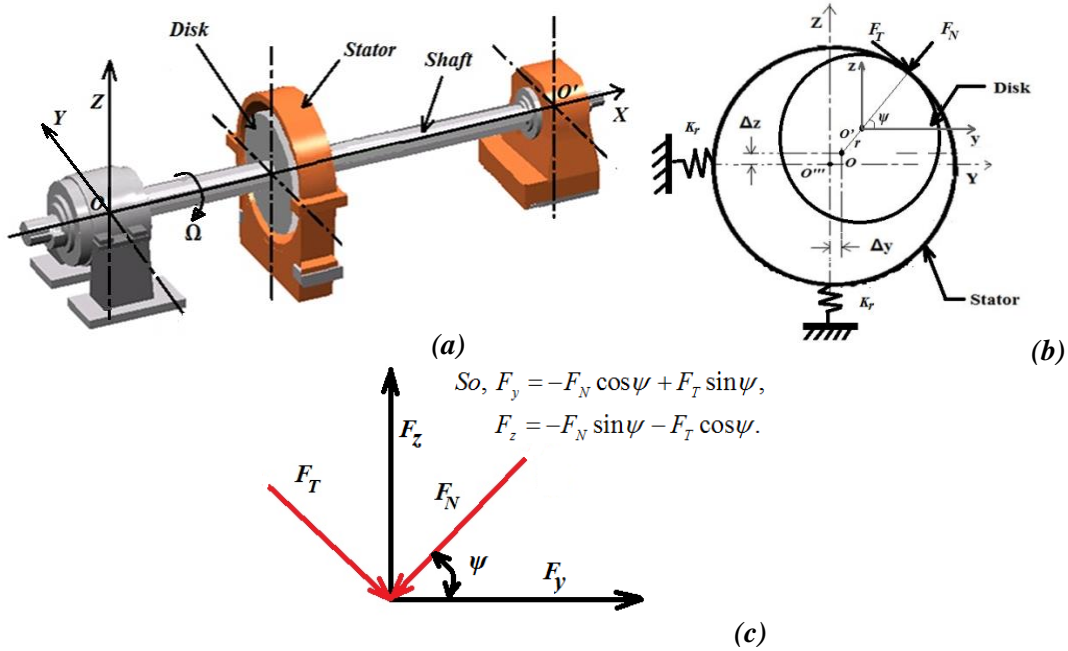
(a)

(b)

(c)

Fig.4.58: a) A rotating system b) Rotor-stator interaction and c) Force analysis of rub impact phenomenon

The shaft is simply supported using the rigid bearings with the condition of inextensibility. An unbalance mass (m_u) has been introduced in the system with an eccentric location r_1. Global coordinate system X-Y-Z is fixed at the left end of the shaft with X-direction along the shaft length while coordinate system x-y-z is a rotating system of coordinate with x direction along the shaft length. Primary excitation to the system is considered due to presence of the unbalance mass. The unbalance force at a high-speed causes large deformation in the shaft and results in rub between the disk and the envelope (stator). The envelope mounted around the rotating system and its center has a small eccentricity (Δv and Δw) from the axis of the rotor system in y and z-directions, respectively. The clearance δ is between the stator and disk as shown in Fig.4.58. When the displacement of the disk (i.e r) exceeds the clearance δ, the rub between stator and disk happens. During the rubbing, the stator surface applies radial force F_n and tangential force F_t on the disk. Here, the rubbing assumed to be a stick-free phenomenon and rolling of the disk over the stator surface without affecting the whirling of the rotating system is considered. Thus, the radial force and tangential force can be written as.

$$F_n = \begin{cases} K_r(r-\delta) & r > \delta \\ 0 & r < \delta \end{cases} \quad \text{and} \quad F_t = \eta F_n.$$

$$\text{Here,} \quad r = \left(\sqrt{(v-\Delta v)^2 + (w-\Delta w)^2} \right)\Big|_{x=L_d}. \tag{4.38}$$

Here, K_r is radial stiffness of the rotor and η is the coefficient of friction. Therefore, the tangential and radial forces can be written in y and z direction as

$$\begin{cases} F_x = K_r(1-\delta/r)\{(v-\Delta v) - \eta(w-\Delta w)\}\big|_{x=L_d} \\ F_y = K_r(1-\delta/r)\{\eta(v-\Delta v) + (w-\Delta w)\}\big|_{x=L_d} \end{cases} \quad \text{if } r \geq \delta$$

$$F_x = 0, \quad F_y = 0, \qquad \qquad \text{if } r < \delta \tag{4.39}$$

When the radial displacement of the disk (r) is less than the clearance (δ), then there is no rub condition. Considering the rub impact force model which is described in Eq.(4.39), the partial differential equation motion of the rotating system (i.e. Eqs.(4.9)-(4.10)) can be modified as

$$m(v_{tt} + v_{xx}\int_1^x\int_0^x(v_{xt}^2 + v_{xtt}v_x + w_{xt}^2 + w_{xtt}w_x)dxdx + v_x\int_0^x(v_{xt}^2 + v_{xtt}v_x + w_{xt}^2 + w_{xtt}w_x)dx) + cv_t$$

$$-I_2(2\Omega w_{xxt} + v_{xxtt}) + D_{22}(v_x^2 v_{xxxx} + v_x w_x w_{xxxx} + 3v_x w_{xx} w_{xxx} + v_{xx}w_x^2 + v_x^3 + v_{xxxx} + w_x v_{xx}w_{xxx}$$

$$+4v_x v_{xx}v_{xxx}) - I_{2d}(2\Omega w_{xxt} + v_{xxtt})\big|_{x=L_d} + M(v_{tt} + v_{xx}\int_1^x\int_0^x(v_{xt}^2 + v_{xtt}v_x + w_{xt}^2 + w_{xtt}w_x)dxdx)\big|_{x=L_d}$$

$$+M(v_x\int_0^x(v_{xt}^2 + v_{xtt}v_x + w_{xt}^2 + w_{xtt}w_x)dx)\big|_{x=L_d} = m_u\Omega^2 r_1\cos\Omega t + F_y. \tag{4.40}$$

$$m(w_{tt} + w_{xx}\int_1^x\int_0^x(v_{xt}^2 + v_{xtt}v_x + w_{xt}^2 + w_{xtt}w_x)dxdx + w_x\int_0^x(v_{xt}^2 + v_{xtt}v_x + w_{xt}^2 + w_{xtt}w_x)dx) + cw_t$$

$$+I_2(2\Omega v_{xxt} - w_{xxtt}) + D_{22}(w_x^2 w_{xxxx} + w_x v_x v_{xxxx} + 3w_x v_{xx}v_{xxx} + w_{xx}v_x^2 + w_{xx}^3 + w_{xxxx} + v_x w_{xx}v_{xxx}$$

$$+4w_x w_{xx}w_{xxx}) + +M(w_{tt} + w_{xx}\int_1^x\int_0^x(v_{xt}^2 + v_{xtt}v_x + w_{xt}^2 + w_{xtt}w_x)dxdx)\big|_{x=L_d} +$$

$$M(w_x\int_0^\zeta(v_{xt}^2 + v_{xtt}v_x + w_{xt}^2 + w_{xtt}w_x)dx)\big|_{x=L_d} + I_{2d}(2\Omega v_{xxt} - \ddot{w}_{xxtt})\big|_{x=L_d} = m_u\Omega^2 r_1\sin\Omega t + F_z. \tag{4.41}$$

Galerkin's method and first mode of discretization:

The rotating system (Fig.4.58) is simply supported using the rigid bearings. Thus, similarly $\varphi(x)$ which is expressed as $\varphi(x) = \sqrt{2}\sin(\pi x / L)$ in the previous section is the linear eigenfunction for the present shaft. Then, the equations of motion for the rotating system can be then expressed as

$$m(\varphi v_{tt} + v(v_t^2 + v_{tt}v + w_t^2 + w_{tt}w)\varphi_{xx}\int_L^x\int_0^x\varphi_x^2 dxdx + v(v_t^2 + v_{tt}v + w_t^2 + w_{tt}w)\varphi_x\int_0^x\varphi_x^2 dx)$$

$$+D_{22}(\varphi_{xxxx}v + (\varphi_x^2\varphi_{xxxx} + \varphi_{xx}^3 + 4\varphi_x\varphi_{xx}\varphi_{xxx})v^3 + (\varphi_x^2\varphi_{xxxx} + 3\varphi_x\varphi_{xx}\varphi_{xxx} + \varphi_{xx}^2\varphi_{xx} + \varphi_x\varphi_{xx}\varphi_{xxx})w^2 v)$$

$$+M\left(\varphi_d v_{tt} + v(v_t^2 + v_{tt}v + w_t^2 + w_{tt}w)\varphi_{dxx}\int_L^x\int_0^x\varphi_{dx}^2 dxdx + v(v_t^2 + v_{tt}v + w_t^2 + w_{tt}w)\varphi_{dx}\int_0^x\varphi_{dx}^2 dx\right)\bigg|_{x=L_d}$$

$$-\varphi_{xx}I_2(2\Omega w_t + v_{tt}) + \varphi c\dot{v} - I_{2d}\varphi_{dxx}(2\Omega w_t + v_{tt})\big|_{x=L_d}) = m_u\Omega^2 r_1\varphi_d\cos\Omega t + F_y. \tag{4.42}$$

$$m(\varphi w_{tt} + w(v_t^2 + v_{tt}v + w_t^2 + w_{tt}w)\varphi_{xx}\int_L^x\int_0^x\varphi_x^2 dxdx + w(v_t^2 + v_{tt}v + w_t^2 + w_{tt}w)\varphi_x\int_0^x\varphi_x^2 dx)$$

$$+D_{22}(\varphi_{xxxx}w + (\varphi_x^2\varphi_{xxxx} + \varphi_{xx}^3 + 4\varphi_x\varphi_{xx}\varphi_{xxx})w^3 + (\varphi_x^2\varphi_{xxxx} + 3\varphi_x\varphi_{xx}\varphi_{xxx} + \varphi_{xx}^2\varphi_{xx} + \varphi_x\varphi_{xx}\varphi_{xxx})v^2 w)$$

$$+M\left(\varphi_d w_{tt} + w(v_t^2 + v_{tt}v + w_t^2 + w_{tt}w)\varphi_{dxx}\int_L^x\int_0^x\varphi_{dx}^2 dxdx + w(v_t^2 + v_{tt}v + w_t^2 + w_{tt}w)\varphi_{dx}\int_0^x\varphi_{dx}^2 dx\right)\bigg|_{x=L_d}$$

$$+\varphi_{xx}I_2(2\Omega v_t - w_{tt}) + \varphi cw_t + I_{2d}\varphi_{dxx}(2\Omega v_t - w_{tt})\big|_{x=L_d}) = m_u\Omega^2 r_1\varphi_d\sin\Omega t + F_z. \tag{4.43}$$

Following dimensionless parameters have further been used for reconstructing the equations of motion towards the non-dimensional form.

$$x^* = \frac{x}{\delta}, \quad v^* = \frac{v}{\delta}, \quad v^* = \frac{w}{\delta}, \quad L^* = \frac{L}{\delta}, \quad \Omega^* = \sqrt{\frac{k_1 m\delta^4}{k_2 D_{22}}}\Omega, \quad t^* = \sqrt{\frac{k_2 D_{22}}{mk_1\delta^4}}t, \quad M_e = \frac{m_u\varphi_d r_1}{mk_1}, \quad I_2^* = \frac{I_2}{m\delta^2},$$

$$I_{2d}^* = \frac{I_{2d}}{m\delta^3}, \quad c^* = \frac{ck_3}{\sqrt{D_{22}mk_1 k_2}}, \quad \Delta y^* = \frac{\Delta y}{\delta}, \quad \Delta z^* = \frac{\Delta z}{\delta}, \quad R = \frac{r}{\delta}, \quad K_r = \frac{D_{22}K_2}{K_r\delta^4}, \quad M = \frac{M}{m\delta}. \tag{4.44}$$

Substitution of the above transformation values in Eqs.(4.42)-(4.43), it results in following non-dimensional governing equations. While *Asterisk has been dropped for the sake of simplicity*

$$v_{tt} + v + cv_t - \frac{2k_4}{k_1}\Omega w_t + \frac{k_5}{k_2}(v^3 + vw^2) + \frac{k_6}{k_1}(vv_t^2 + v_{tt}v^2 + vw_t^2 + vww_{tt}) = M_e\Omega^2\cos\Omega t + f_y. \tag{4.45}$$

$$w_{tt} + w + cw_t + \frac{2k_4}{k_1}\Omega v_t + \frac{k_5}{k_2}(w^3 + v^2 w) + \frac{k_6}{k_1}(wv_t^2 + v_{tt}vw + ww_t^2 + w_{tt}w^2) = M_e\Omega^2\sin\Omega t + f_z. \tag{4.46}$$

Associated boundary conditions:

$$v = 0, \quad v'' = 0, \quad w = 0, \quad w'' = 0. \text{ at } x = 0 \text{ and } x = L. \tag{4.47}$$

Here, coefficients ($k_{1,2\cdots6}$, f_y and f_z) can be expressed as

$$k_1 = \int_0^L (\varphi^2 - I_2\varphi\varphi'' + \beta_1\varphi_d^2 - I_{2d}\varphi_d\varphi_d'')dx, \quad k_2 = \int_0^L \varphi\varphi'''dx, \quad k_3 = \int_0^L \varphi^2 dx,$$

$$k_4 = \int_0^L (I_2\varphi\varphi'' + I_{2d}\varphi_d\varphi_d'')dx, \quad k_5 = \int_0^L \varphi(\varphi'^2\varphi'''' + 4\varphi'\varphi''\varphi''' + \varphi''^3)dx,$$

$$k_6 = \int_0^L (\varphi\varphi''\int_L^x\int_0^x \varphi'^2 dxdx + \varphi\varphi'\int_0^x \varphi'^2 dx + \beta_1(\varphi_d\varphi_d''\int_L^x\int_0^x \varphi_d'^2 dxdx + \varphi_d\varphi_d'\int_0^x \varphi_d'^2 dx))dx,$$

$$\begin{cases} f_y = -(1/K_r)(1-1/R)\{(v-\Delta v)-\eta(w-\Delta w)\}\big|_{x=L_d} \\ f_z = -(1/K_r)(1-1/R)\{\eta(v-\Delta v)+(w-\Delta w)\}\big|_{x=L_d} \end{cases} \qquad \text{if } R \geq 1$$

$$f_y = 0, \quad f_z = 0, \qquad\qquad\qquad\qquad\qquad \text{if } R < 1$$

Here, $R = \left(\sqrt{(v-\Delta v)^2 + (w-\Delta w)^2}\right)\big|_{x=L_d}$ .This is simplified form of the nonlinear equations of motion which accommodates the effect of geometric nonlinearity terms $(v^3 + vw^2)/(w^3 + v^2 w)$, effect of inertial nonlinearity terms $(vv_t^2 + v_{tt}v^2 + vw_t^2 + vww_{tt})/wv_t^2 + v_{tt}vw + ww_t^2 + w_{tt}w^2$, effect of rub impact terms f_y/f_z and forcing terms $M_e\Omega^2\cos\Omega t$ in planes x-y and x-z, respectively.

4.5.2 Result and Discussion

We here analyze the effect of rub-impact between the rotating shaft and the stator on the dynamic behavior with the system parameters are taken as shaft length ($L = 0.8\ m$), disk position ($L_d = L/3$), Non-dimensional disk mass ($M=1.5$), non-dimensional unbalance mass ($M_e=0.15$), eccentricities of the stator axis relative to the axis of the rotor are $\Delta v =0.2$ and $\Delta w=0.85$ in y and z directions respectively. The coefficient of friction of the rubbing surface is assumed to be 0.2 while the clearance between the stator and the rotor is taken as 0.005.

The spin speed is the most essential parameter that has a substantial effect on the dynamic behavior of the system. Figure 4.59 shows a bifurcation diagram to evaluate the nonlienar behavior of the system with the spin speed (Ω) as a control parameter accounting the rub-impact phenomena. This diagram highlights an insight of rubbing effect on the system behavior when the rotataing shaft is operated between Ω = 2.3 to 3.1.
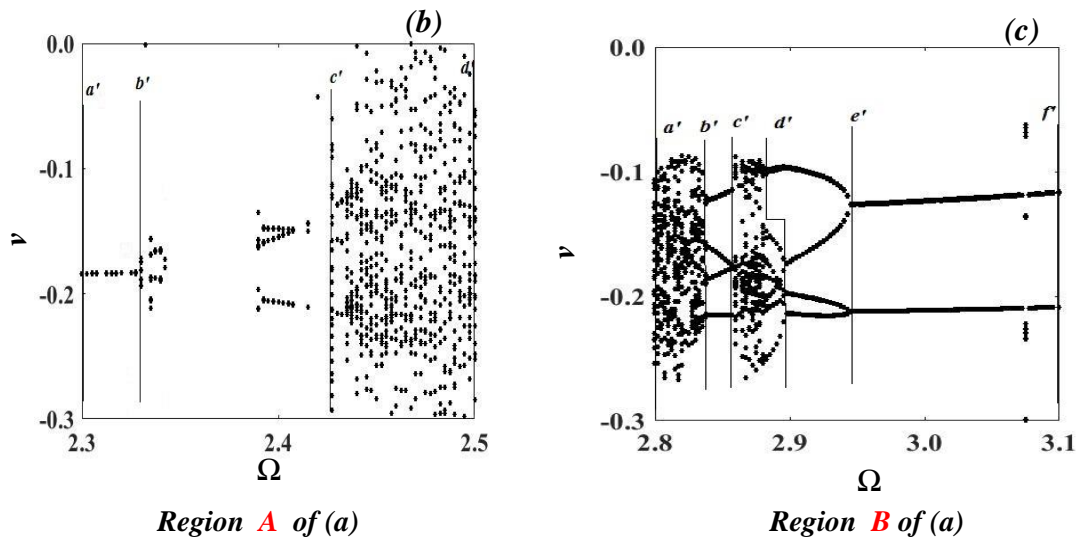

(a)

(b)

Region **A** of (a)

(c)

Region **B** of (a)
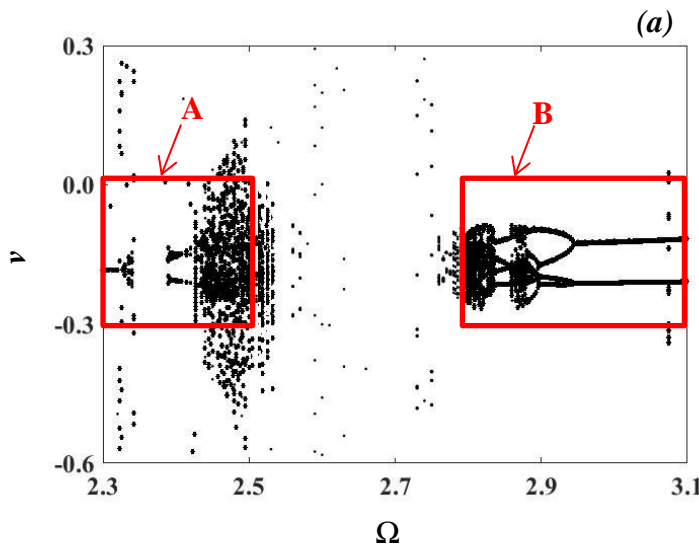
Fig.4.59: Bifurcation Diagram: Effect of spin speed (Ω)

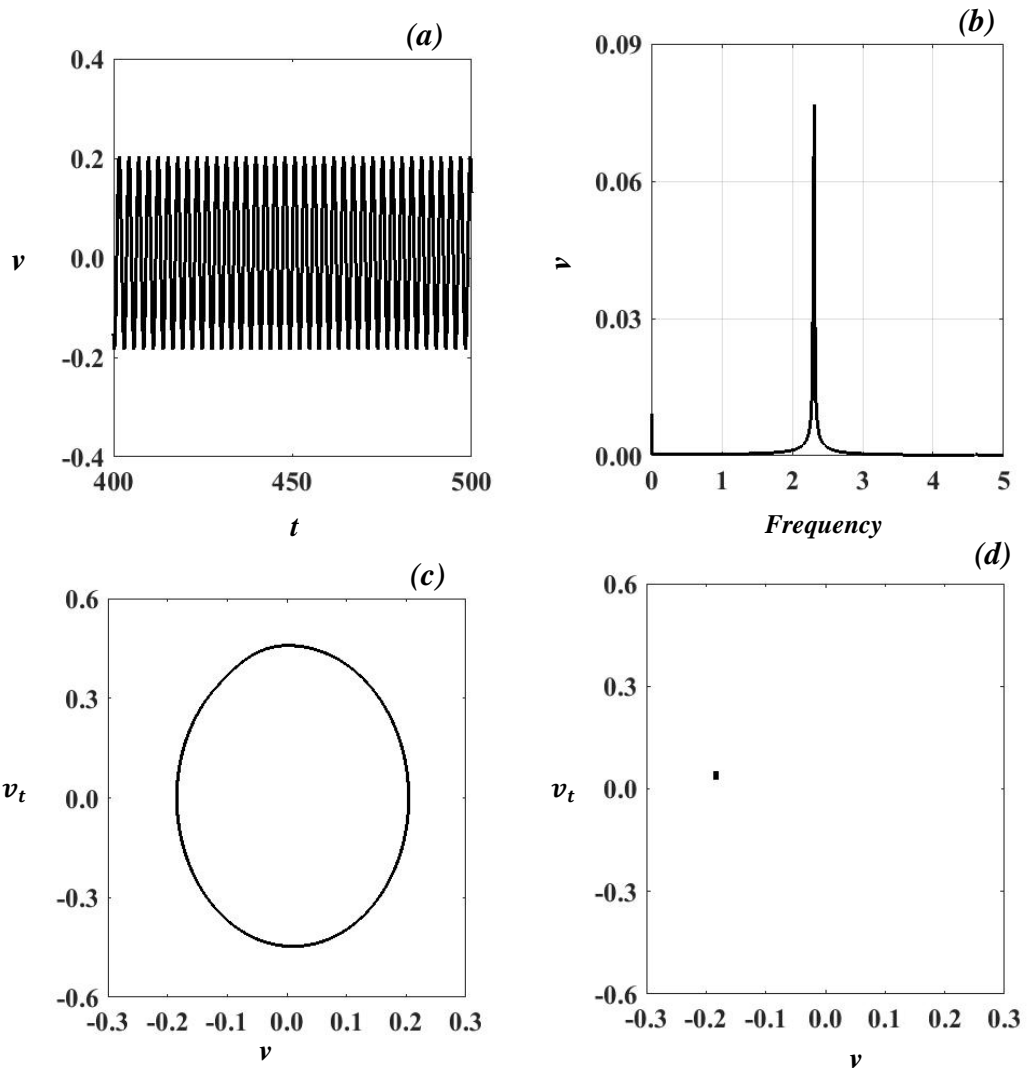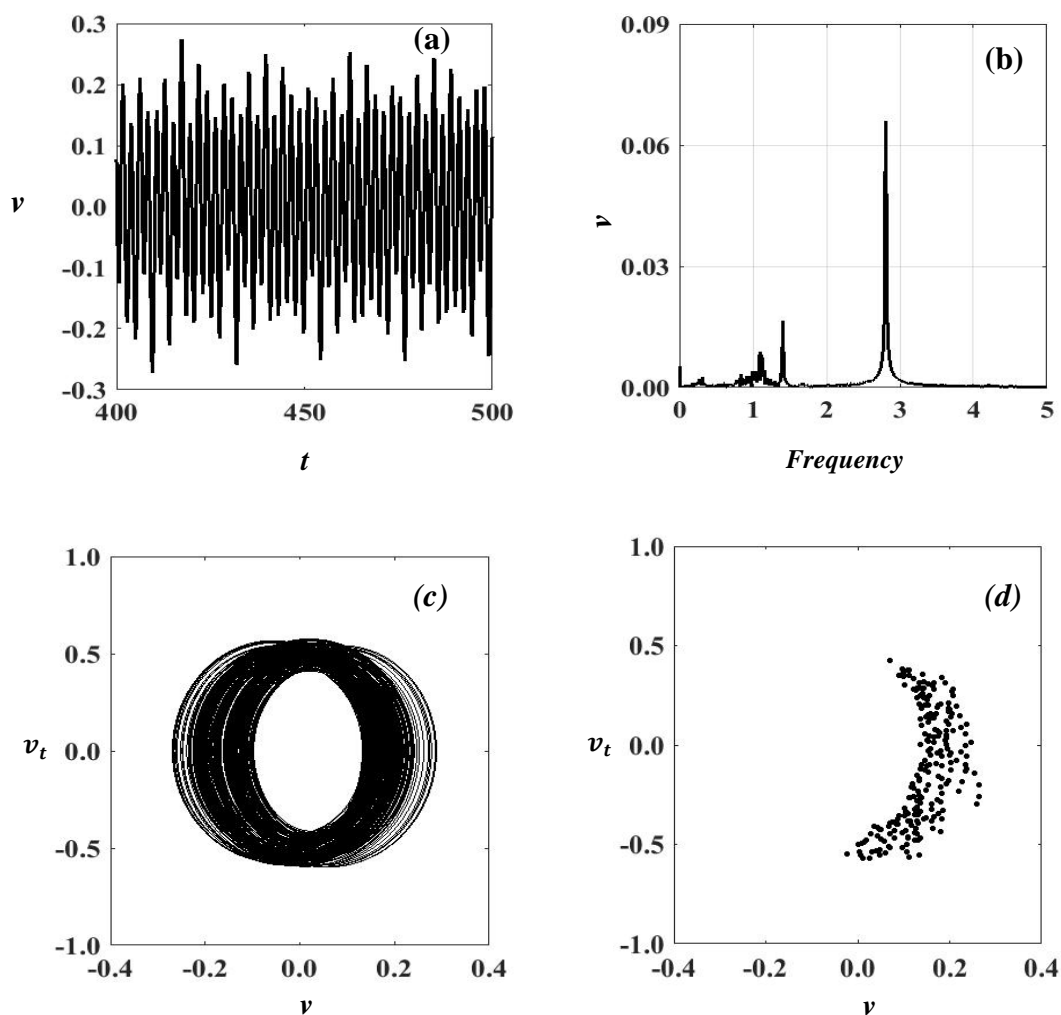**Fig.4.60:** Effect of spin speed a) Time series b) FFT c) Phase portrait map d) Poincare' map : Ω= 2.3.

While at Ω=2.8, the system undergoes chaotic behavior, with further increase in the rotating speed i.e. When rotating speed is at 2.84, the choatic responses gets transformed into multi-periodic behavior. With further increase in the rotating speed, the system finally reach to quasiperidic behaviour followed by period-doubling. From this diagram, it is clear that the

99

system exhibits choatic or multi-peridoic responses due to the presnece of rub-impact that exist when the rotating speed is in between 2.8 and 2.9. Hence, it is adviced to the operator that the shaft speed (Ω) must be kept always more than 2.9 in order to avoid the nonlinear behaviour due to rub between the shaft and stator.

Figure 4.61 shows time history when the rotor runs at a spin speed equal to 2.8. The irregular time series with one peak indicating rotating speed and cluster of peaks near 1 renders a sign of the chaotic behaviours that is further turned into cluster of many points on the Poincare's map. This exhibits a symbol of the chaotic responses at the spin speed Ω=2.8. With further increase in the spin speed to 3, the double periodic behavior is observed that shows beating phenomenon in the time series with the steady state response. The corresponding FFT shows the effect of two frequency, i.e., ω = 3 and 1.5. The ω = 3 depicts the effect of spin speed (Ω) but there is a rise of unknown frequency ω = 1.5 which is almost half of the spin speed. A loop in trajectory of the phase portrait with two points on the Poincare's map can be observed clearly, these observation depict double periodic behavior of the system at spin speed Ω =3.

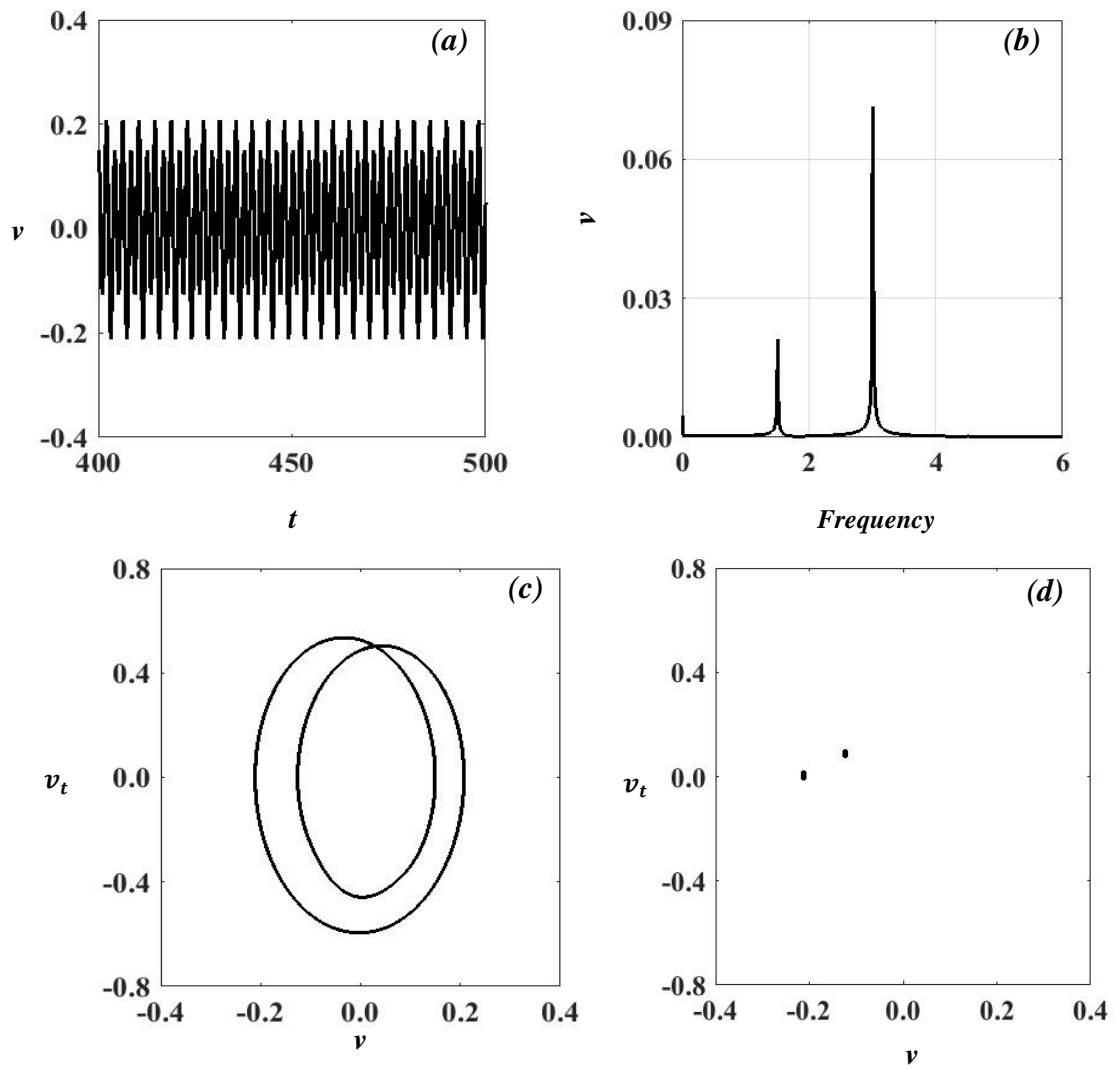**Fig.4.61:** Effect of spin speed a) Time series b) FFT c) Phase portrait map d) Poincare' map : Ω= 2.8.

Fig.4.62: Effect of spin speed a) Time series b) FFT c) Phase portrait map d) Poincare' map : Ω = 3.
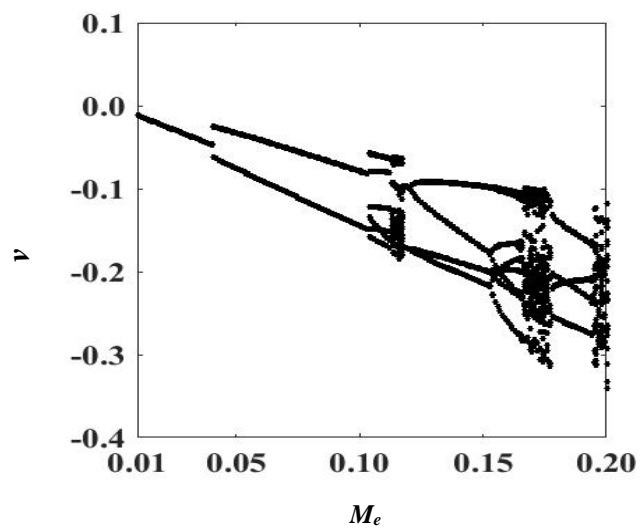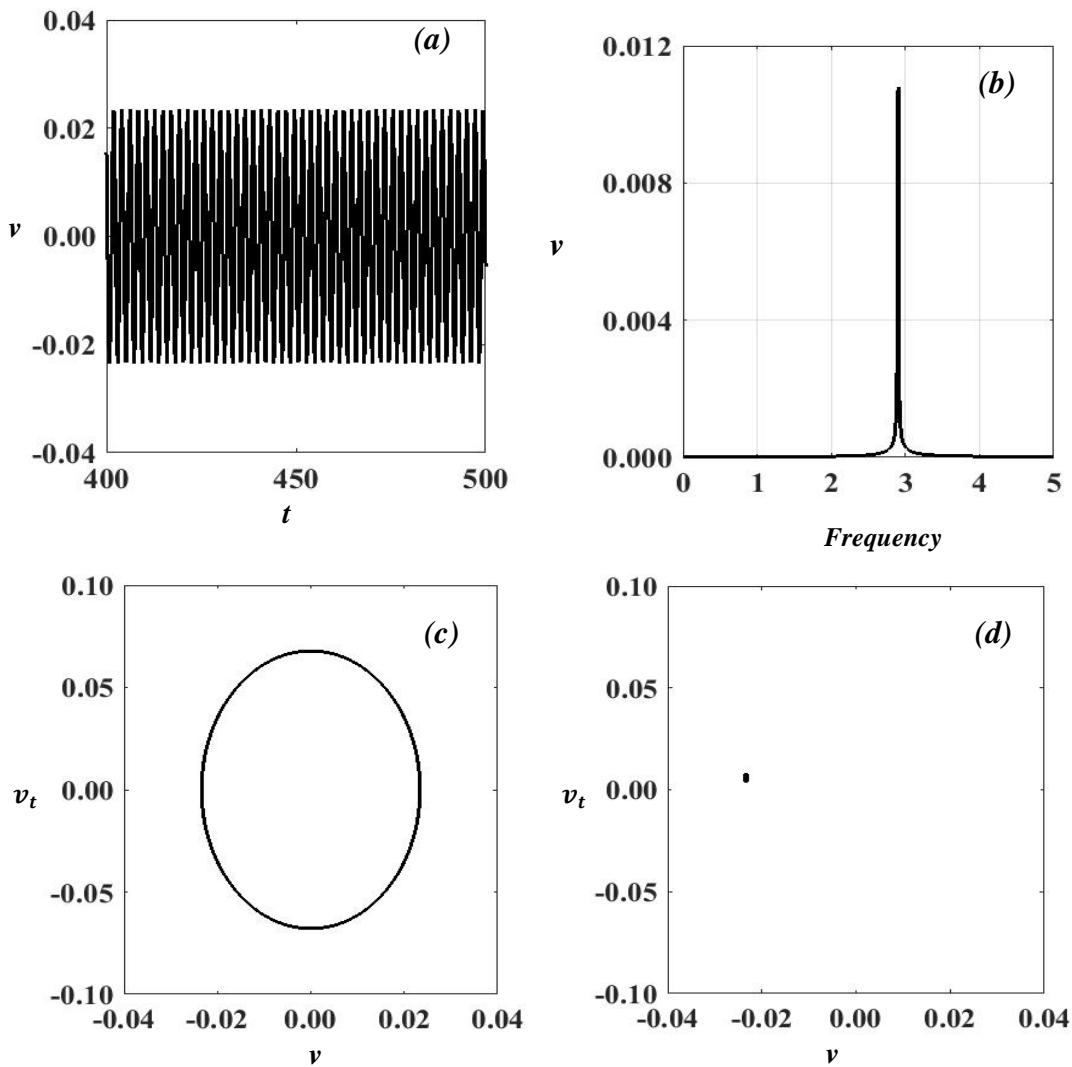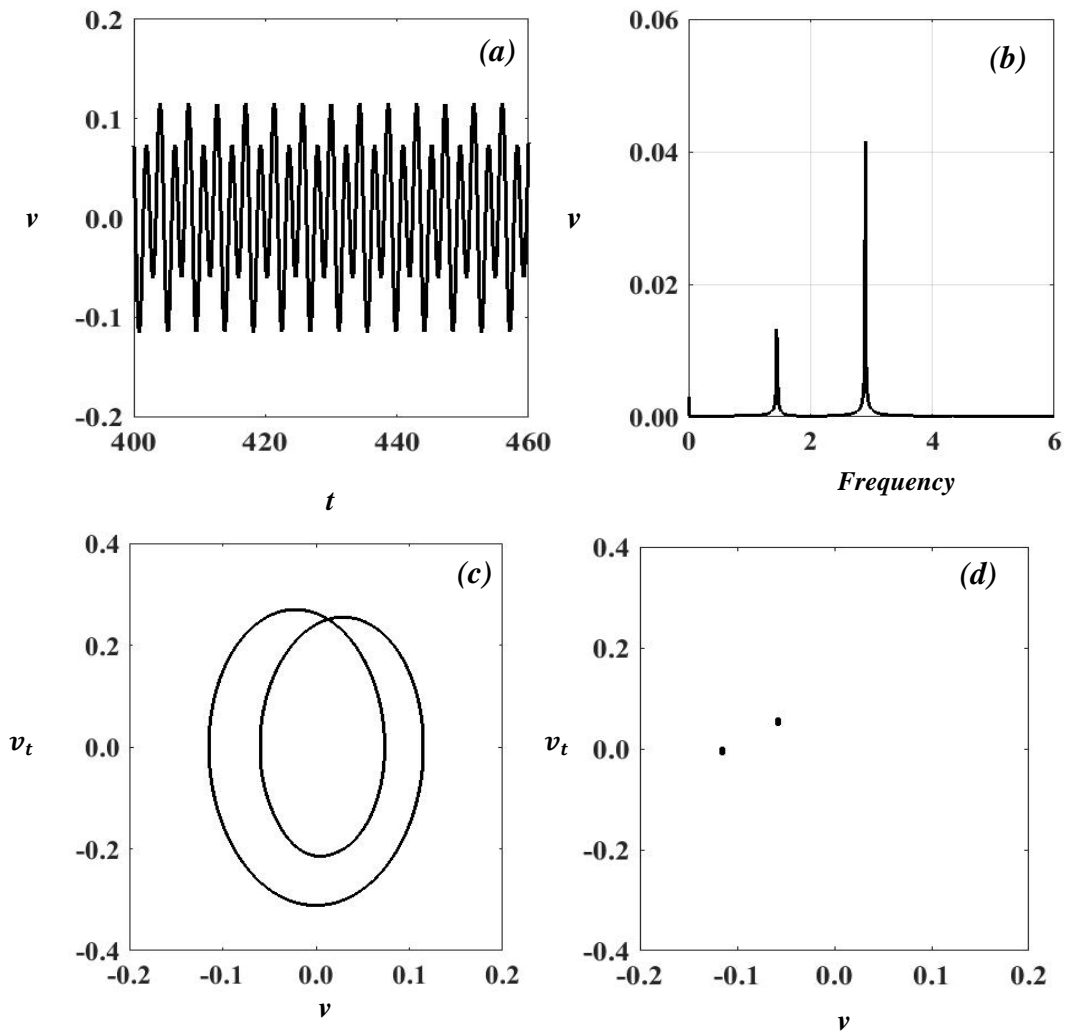

Fig.4.63: Bifurcation Diagram: Effect of unbalance mass (M_e)

Fig.4.64: Effect of unbalance mass a) Time series b) FFT c) Phase portrait map d) Poincare' map : M_e= 0.02.

Since a mechanical unbalance is found to be a primary fault in the rotating system, the system performance and operation stability largely depends on this destabalized parameter. The system performance becomes more complex and critical when both the mass unbalance and the rub-impact occur together. Thus it is necessary to analyze the effect of the unbalance with rubbing phenomenon. Figure 4.63 shows a bifurcation diagram for the system behavior with the unbalance mass (M_e) as a control parameter. The route to chaos phenonmenon can be observed in the bifurcation diagram. The figure shows a period doubling behavior at M_e =0.042 and then it merges into a chaotic behavior when the M_e equals to 0.113. With further increase in the M_e to 0.118, the chaotic behavior turns into double-periodic behavior. Then it repeats the rout to chaos phenomena again with further increase in the M_e. For the range of M_e= 0.01 to 0.2, the route to chaos is repeated three times. Hence, the presence of the mass unbalance makes the system highly unstable and should be kept away as much as possible.

Figures 4.64–4.66 illustrates steady state response of the rotating system obtained numerically integrating the equation of motion (Eqs. (4.45)-(4.46)) at various values of the mass unbalance. While a peridic reponses is observed at M_e = 0.02, but, when the M_e increases to 0.08, the system undergoes double-periodic behavior arising due to the rise of half frequency to that of the spin speed. With further increase in the M_e to 0.175, the system may lead to chaotic behaviour nature, as shown in Fig.4.66; this may lead to catastrophic failure or damage to a system.

Fig.4.65: Effect of unbalance mass a) Time series b) FFT c) Phase portrait map d) Poincare' map : M_e= 0.08.

Effect of change in the coefficient of friction on the rotating system behavior can be observed from Figs.4.67–4.69. The bifurcation diagram (Fig.4.67) is derived at spin speed Ω = 2.9. the system shows four branches at η =0.01 and these branches cross at η =0.105. The cross point looks similar to a single periodic motion. Further increase in the η results in two branches and which are corresponding to double periodic behavior.
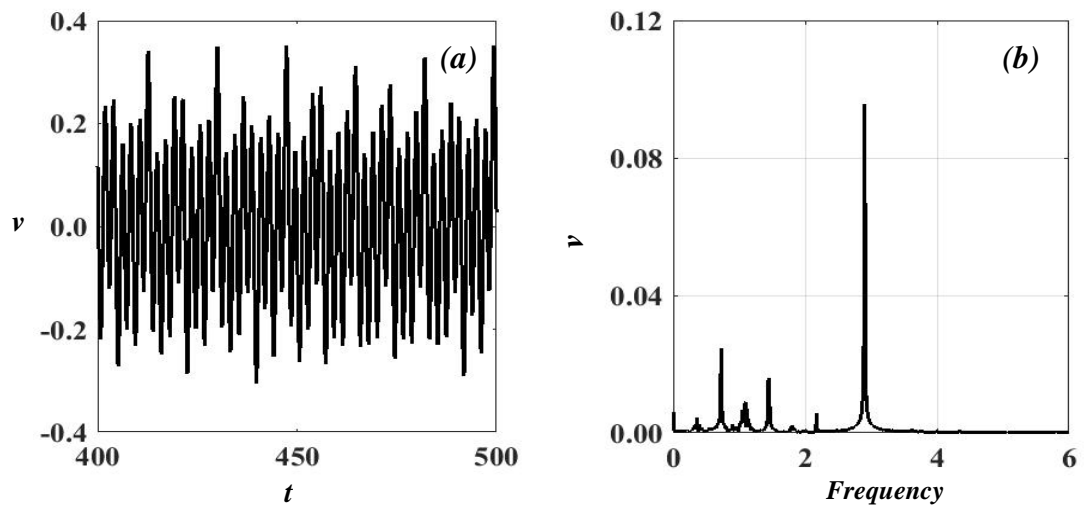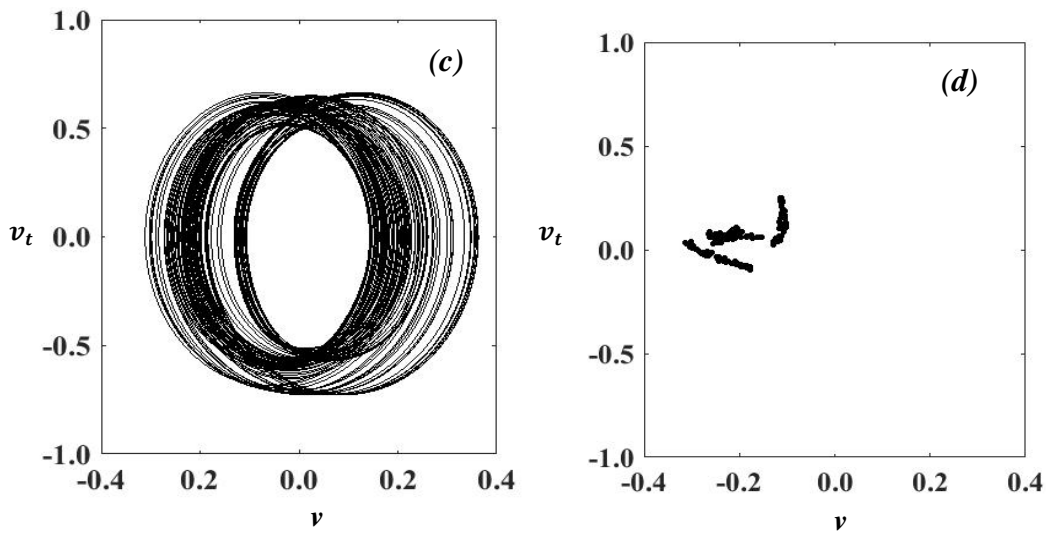
Fig.4.66: Effect of unbalance mass a) Time series b) FFT c) Phase portrait map d) Poincare' map : M_e= 0.175.
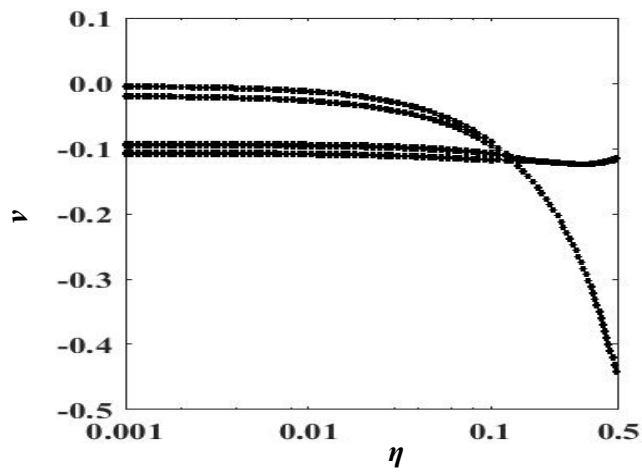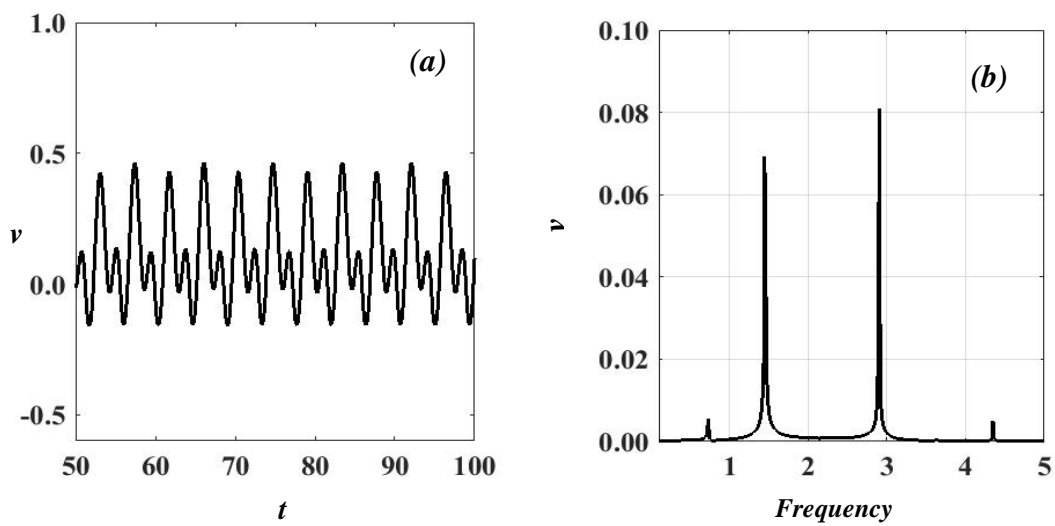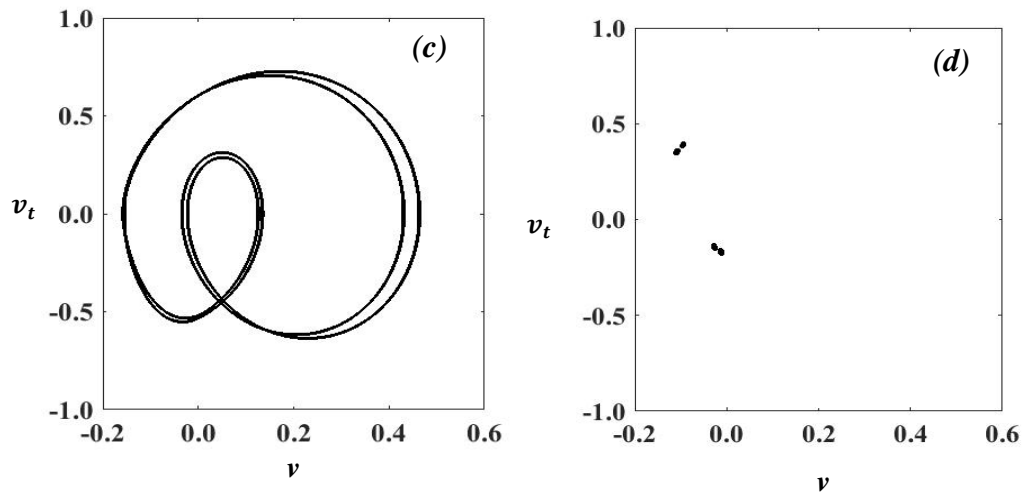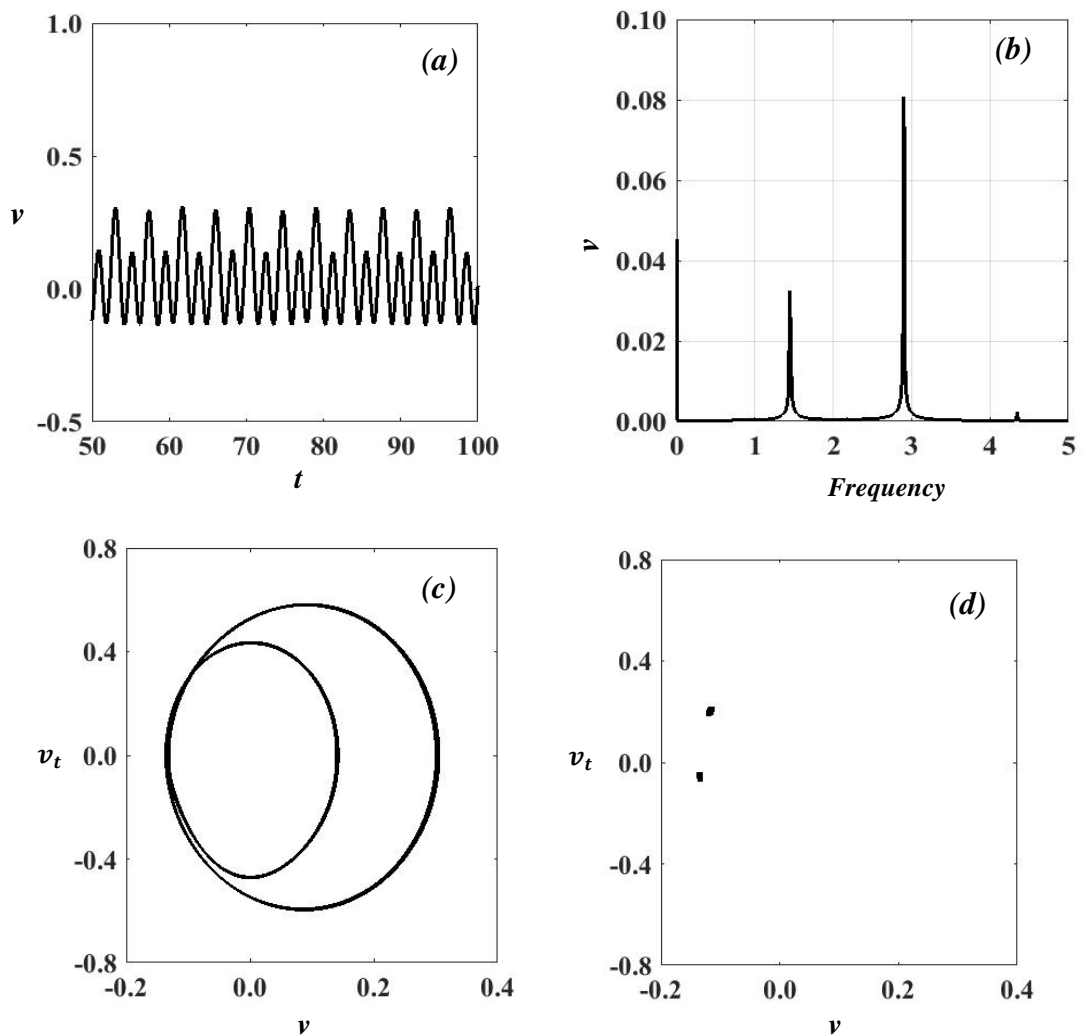

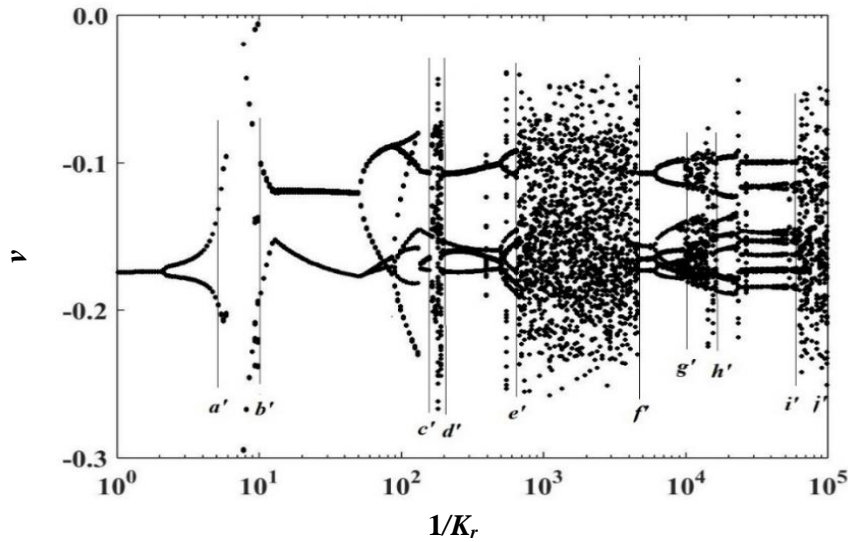**Fig.4.67:** Bifurcation diagram: Effect of coefficient of Friction (η)

Fig.4.68: Effect of coefficient of Friction a) Time series b) FFT c) Phase portrait map d) Poincare' map :η =0.01.


Fig.4.69: Effect of coefficient of Friction a) Time series b) FFT c) Phase portrait map d) Poincare' map : η =0.15.

Figure 4.68 shows four points on the Poincare's map with two loops of a closed trajectory. It depicts four periodic behavior of the system at η = 0.01. If the η is increased to 0.15 value, two points on the Poincare's map with one loop on the phase portrait are observed. It depicts double periodic behavior of the system in Fig 4.69.

Fig.4.70: Bifurcation Diagram: Effect of stifness of rub surface (i.e stator) $1/K_r$

Evaluation of the system behavior with a change in the $1/K_r$ as a control parameter is portrayed in Fig.4.70. The figure shows a route to chaos phenomena multiple times in the range of $1/k_r = 0.01$ to $1{\times}10^5$. The bifurcation diagram (Fig.4.70) shows instability region (*a'- b'*) with derange response amplitude and chaotic region (*c'- d', e' – f', g' – h'* and *i' – j'*). The system almost loses stability in a region between 4 to 10.3 values, and it may lead to catastrophic failure also. The system shows periodic behavior as shown in Fig.4.70 at *1/K_r* =0.0167. This behavior further transformed into double periodic at 10.4 and remain the same till to 14. Figure 4.71 shows a perodic behavior of the system at $1/K_r$ =0.0167 with reference to a periodic range of the bifurcation diagram. One of the values from the double periodic range is evaluated in Fig.4.72 and the beat phenomenon in the time series, two peaks on the FFT , a loop in the phase portrait and two points in the Poincare's map are observed at $1/K_r$ =3.34. The chaotic behavior is also observed, when the system behavior is analysed at $1/k_r$ =2.67$\times10^3$, as shown in Fig.4.73. The scattered points on the Poincare's map and the irregular pattern in the time series map depict chaotic nature of the system.
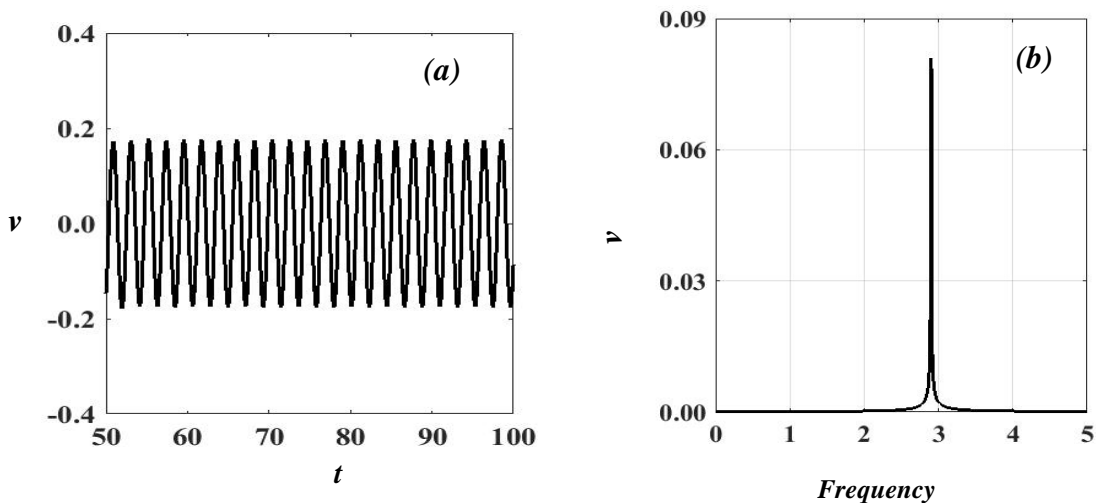
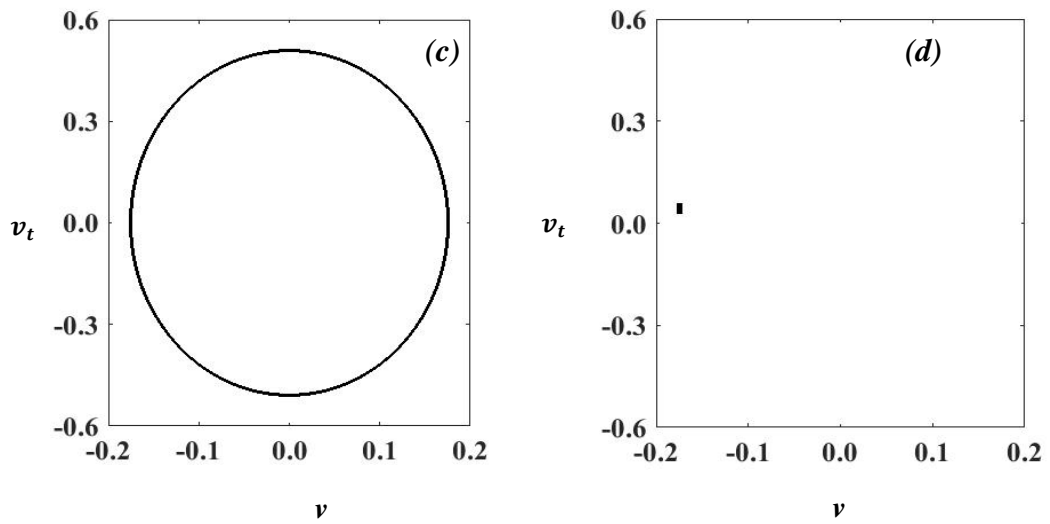**Fig.4.71:** Effect of stifness of rub surface a) Time series b) FFT c) Phase portrait map d) Poincare' map : 1/K$_r$ =0.0167.
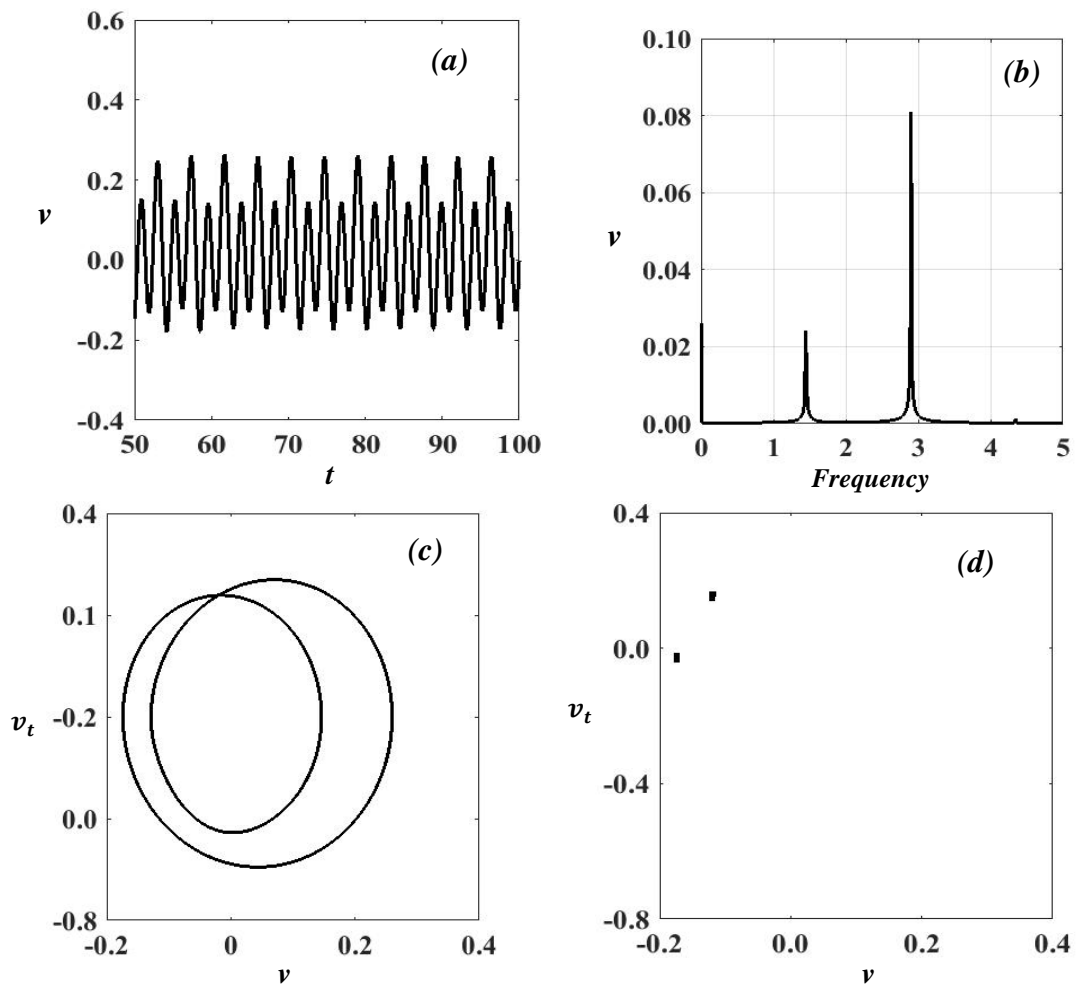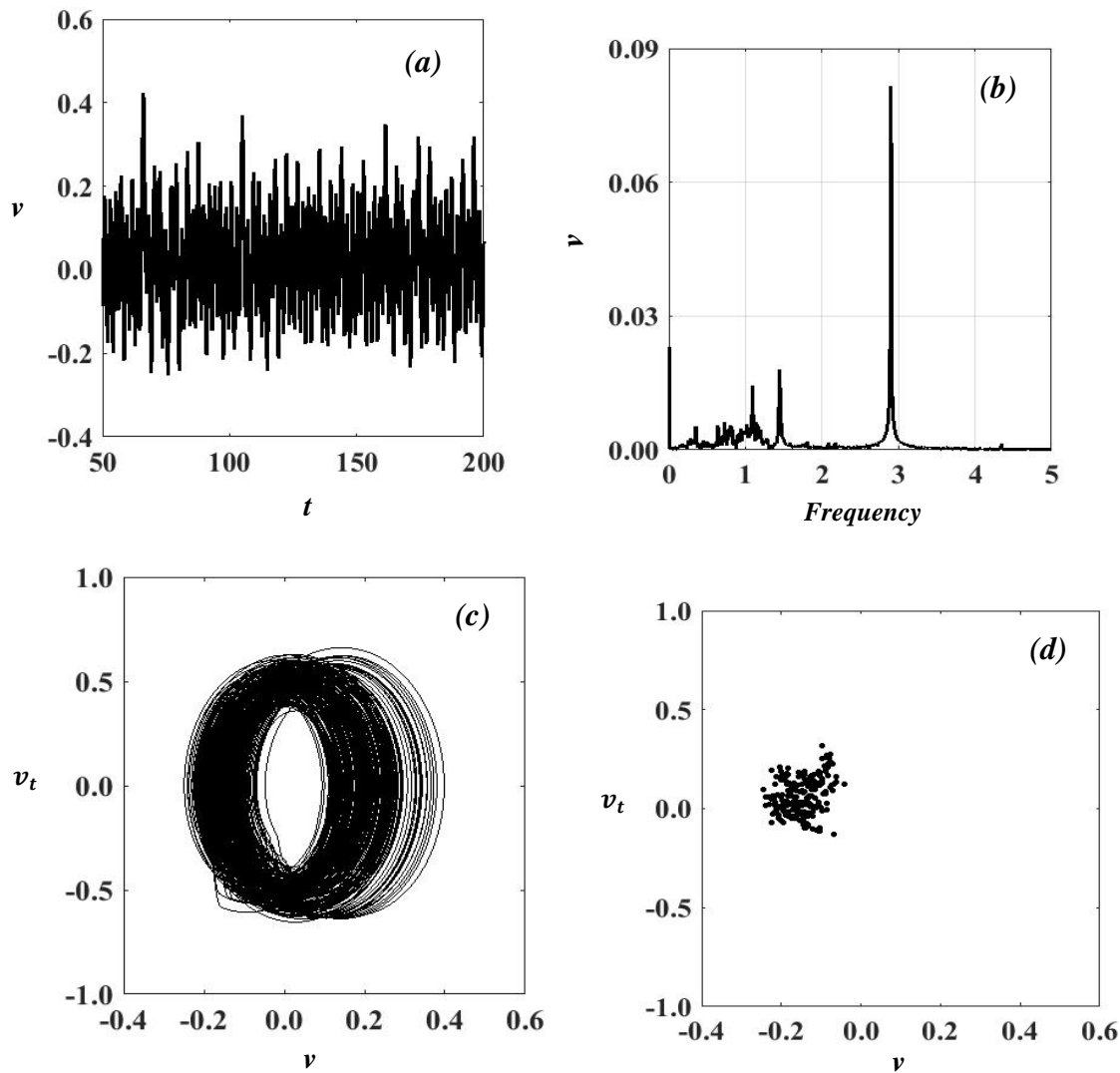

Fig.4.72: Effect of stifness of rub surface a) Time series b) FFT c) Phase portrait map d) Poincare' map : 1/K$_r$ =3.34.

107

Fig.4.73: Effect of stifness of rub surface a) Time series b) FFT c) Phase portrait mapd) Poincare' map : $1/K_r$ =2.67×10^3.

4.6 Summary

The rotating shaft-disk system with the rotary inertia, gyroscopic effect and nonlinear curvature has been analyzed for determining the natural frequencies and resulting free vibration response under the influences of various control parameters. The rotary inertia and gyroscopic effect combined with the inextensible geometric condition for the pinned-guided shaft element have been taken into account to develop the governing equation of motion. The closed-form mathematical expressions have been derived for determining both the linear and nonlinear natural frequencies and their behavioral patterns have been simultaneously demonstrated through time histories, FFTs and Poincare's maps upon changing the control parameters.

A well-known perturbation method i.e. the method of multiple scales is used to obtain the solution of the nonlinear equation of motion. Moreover, the results obtained numerically and perturbation analysis are compared and found in compliance. The results for the system with the disk are compared with that of the shaft alone and it has found to have a lower natural frequency and first node appears before as it appears for the shaft the for lower spin speed.

Nonlinear whirling speed has been observed to be higher about 5-8% as compared to the findings via the linear analysis. The variation of linear frequencies with the location of the disk denoted that with the disk moving away from the center, the rate of increase of the frequency

increases. It has also been observed that the initial conditions play an important role in obtaining the nonlinear natural frequencies of the rotor-bearing system.

Further, a large deflection model of the flexible rotor-bearing system which includes a flexible shaft characterized with nonlinear curvature and gyroscopic effect, geometric eccentricity, a rigid disk crooked with unbalance mass, and nonlinear flexible bearings has been developed. Here, nonlinear flexible bearings are being modeled with linear and nonlinear properties of the bearing along with damping component. This typical dynamic model has been developed to study the instability caused due to the imbalance.

A set of nonlinear algebraic equations have been derived by using the method of multiple scale that to govern the overall dynamic behaviour and stability by investigating bifurcation and route to chaos upon changing the design parameters i.e., eccentricity, unbalance and disk parameters under resonance conditions. The system losses its stability due to a sudden change in the response amplitude being present of saddle-node bifurcation and it has been studied in details with the illustration of time history, phase trajectories, bifurcation diagram and Poincare's map for the each category

The behavior of the system can be successfully controlled with an appropriate selection of the geometric eccentricity as well as the possibility of instability and catastrophic failure of the system can also be attenuated. An increase in the shaft speed causes a sharp increase in the vibration amplitude when the disk is located away from the mid-span. For a moderately large value of the disk-mass, a region of the instability improves with a smaller range. The amplitude and the instability range get smaller for a lower value of the unbalance mass and the other way around. However, the change in the unbalance mass does not affect the rate of change of amplitude $dv/d\Omega$. The system showed a decrease in the hardening effect with increase in the mass moment of inertia (M.I).

Consequently, the system has smaller region of the instability for a higher value of the M.I. Finally, the eccentricity strongly exhibits the chaotic behaviors when its value crosses to one of its critical value. The system with flexible bearing support shows less hardening effect but increase in the hardening effect can be observed by considering large value of the nonlinear stiffness coefficient of the bearings.

The rub impact rotor system with the geometrical and inertial nonlinearities is analyzed to investigate its stability and bifurcation behavior. The bifurcation analysis is performed by regulating systems parameters such as spin speed, coefficient of friction, stiffness of the stator surface and unbalance. It is found that the system behavior has substantial effect of variations in these parameters. These variations cause a route to chaos phenomenon in the dynamic behavior of the system. For analyzed range of the parameters, the system shows dominance of a rubbing effect. This nonlinear nature of the system under effect of the rub and the unbalance can lead to instability and then to catastrophic failure or poor performance.